

Assessment of effective-one-body radiation reactions for generic planar orbits

Simone Albanesi^{1,2}, Alessandro Nagar^{2,3}, Sebastiano Bernuzzi⁴, Andrea Placidi^{5,6}, and Marta Orselli^{5,6}

¹ *Dipartimento di Fisica, Università di Torino, via P. Giuria 1, 10125 Torino, Italy*

² *INFN Sezione di Torino, Via P. Giuria 1, 10125 Torino, Italy*

³ *Institut des Hautes Etudes Scientifiques, 91440 Bures-sur-Yvette, France*

⁴ *Theoretisch-Physikalisches Institut, Friedrich-Schiller-Universität Jena, 07743, Jena, Germany*

⁵ *Dipartimento di Fisica e Geologia, Università di Perugia,*

INFN Sezione di Perugia, Via A. Pascoli, 06123 Perugia, Italia and

⁶ *Niels Bohr Institute, Copenhagen University, Blegdamsvej 17, DK-2100 Copenhagen O, Denmark*

(Dated: May 20, 2022)

In this paper we assess the performances of different analytical prescriptions for the effective-one-body (EOB) radiation reaction along generic planar orbits using exact numerical result in the test-mass limit. We consider three prescriptions put forward in the recent literature: (i) the quasicircular prescription (QC), (ii) the QC with second post-Newtonian (2PN) order noncircular corrections (QC2PN), and (iii) the QC corrected by the noncircular Newtonian prefactor (NCN). The analytical fluxes are then compared against the exact fluxes that are computed by solving the Teukolsky equation with a test-mass source in geodesic motion. We find that the NCN prescription is the most accurate for both eccentric and hyperbolic orbits and it is in robust agreement also for large values of the eccentricity. This result carries over to the comparable masses, as we discuss for a numerical-relativity (NR) case study. We also demonstrate that, while the EOB/NR waveform unfaithfulness is a necessary check for the precision of EOB models, the direct comparison of EOB/NR fluxes is a more stringent and informative test to select the best prescription. Finally, we propose an improved radiation reaction, NCN2PN, that includes noncircular 2PN corrections, in resummed form, as a further multiplicative contribution and that is valid for any mass ratio.

I. INTRODUCTION

Motivated by recent observational hints for eccentric and hyperbolic binary black hole mergers in some LIGO-Virgo events [1–3] and by future prospect of detecting binary sources on generic orbits with LISA [4–6], the analytical relativity community has intensified the efforts in building up accurate gravitational-wave (GW) models for *noncircularized* coalescing compact binaries [7–21]. Among the possible approaches, the effective-one-body (EOB) framework [22–26] offers a theoretically complete method for a unified description of different classes of astrophysical binaries, from the comparable masses to the intermediate and extreme-mass-ratio regimes, and for incorporating the fast motion and ringdown dynamics. Together with the Hamiltonian, the key building block of an EOB model is the radiation reaction force, which is currently prescribed by sophisticated analytically resummed expressions building on the circular, factorized EOB waveform of Ref. [27]. The purpose of this work is to assess the performances of different prescriptions for the EOB radiation reaction along generic planar orbits using exact numerical result in the test-mass limit.

The generalization of the quasicircular EOB model **TEOBResumS** [28, 29] to nonquasicircular configurations [9, 10, 12] has allowed the construction of the first, and currently only, waveform model for spin-aligned black hole binaries that can accurately deal with both hyperbolic captures [10, 12, 13, 30, 31] and eccentric inspirals [9, 12, 13]. The model of Refs. [9, 12] has been used to analyze the GW source GW190521 [1, 32] under the hypothesis of a hyperbolic capture [3]. In its latest avatar [13], the **TEOBResumS** model for generic, but pla-

nar, orbital motion displays: (i) an excellent agreement with the 28 numerical relativity (NR) public simulations of eccentric inspirals of the Simulating eXtreme Space-times (SXS) catalog (EOB/NR unfaithfulness mostly around 0.1% except a single outlier $\sim 1\%$) and (ii) a high consistency (maximum disagreement $\sim 4\%$ for the most relativistic configurations) with the only available NR calculation of the scattering angle [33]. Parallel work has extended the quasicircular **SEOBNRv4HM** model to to eccentric inspirals [15, 16, 34, 35] and presented qualitative results for EOB waveforms for hyperbolic encounters [20]. In particular **SEOBNRv4EHM** [20] showed a EOB/NR unfaithfulness mostly around 0.1% for all the 28 numerical relativity datasets available from the SXS collaboration. The EOB radiation reaction consists of an azimuthal component \mathcal{F}_φ and a radial component \mathcal{F}_r . An accurate analytical representation of $(\mathcal{F}_\varphi, \mathcal{F}_r)$ is of paramount importance to correctly track the orbital phase during the inspiral. In the quasicircular case, many years of work eventually brought a highly sophisticated analytical expression of \mathcal{F}_φ , as used in **TEOBResumS**, that incorporates various levels of resummation [27, 36–39]. Key benchmarks for the development of these resummed analytical expressions are the exact fluxes in the test-mass limit that can be numerically computed by solving the Regge-Wheeler or Teukolsky perturbation equations [40–42]. Remarkably, the prescriptions developed in that limit proved reliable *also* when compared with NR-computed fluxes for binaries of comparable masses [43]. Note that such systematic and progressive development in the test-mass regime is absent in the **SEOBNRv4HM** model, whose radiation reaction force has a less sophisticated analytical structure than the **TEOBResumS** one. This might be

one of the reasons behind the fact that the **TEOBResumS** EOB/NR faithfulness for quasicircular, spin-aligned, binaries is, on average, larger by approximately 1 order of magnitude than the **SEOBNRv4EHM** EOB/NR faithfulness. Indeed the larger faithfulness values are obtained for small masses, i.e. during the radiation reaction-dominated inspiral, see Fig. 18 of Ref. [43].

The noncircular radiation reaction of **TEOBResumS** has been developed with the same rationale as the quasicircular one by systematically using the test-mass benchmark [9]. The studies of test-mass flux data of Refs. [9, 14] found that the most reliable analytical representation is given by *dressing* the quasicircular (resummed) quadrupolar flux mode with the leading-order, Newtonian, *generic* (i.e., noncircular) correction factor. This noncircular, Newtonian prescription is indicated here as NCN. An analogous approach can be followed, multipole by multipole, for the waveform [9], which can be further improved by incorporating higher post-Newtonian (PN) corrections as suitably resummed multiplicative factors, as done in Ref. [21] at 2PN accuracy. By contrast, a different approach was taken in the **SEOBNRv4EHM** model [20], that uses the standard quasicircular (QC) azimuthal radiation reaction force \mathcal{F}_φ inherited from the quasicircular **SEOBNRv4HM** model [44, 45], without taking care of explicit nonradial contributions to the loss of angular momentum. Despite the small EOB/NR unfaithfulness found in Ref. [20] for (mild) eccentricities, no dedicated study of the QC radiation reaction in eccentric inspirals was undertaken. Reference [19] computed noncircular corrections up to 2PN order in the waveform that, once incorporated into the QC waveform, constitute another possible prescription for the EOB radiation reaction. We refer to this prescription as QC2PN. The 2PN corrections, though available, were not included Ref. [20] and thus the QC2PN choice remains so far totally untested against numerical data.

This paper aims at assessing the three prescriptions for the EOB radiation reaction: (i) the QC in the noncircular case (as used in **SEOBNRv4EHM** [20]), (ii) the QC2PN proposed in Ref. [19] (not previously implemented in any complete waveform model), and (iii) NCN of Refs. [9, 12, 13] (used in **TEOBResumS**). The analytical fluxes are compared to the exact numerical fluxes emitted at null infinity by a test-particle orbiting along eccentric equatorial orbits in Kerr spacetime, as computed solving the 2+1 Teukolsky equation on hyperboloidal slices [42].

A. Overview of the results

The main result of the paper is illustrated in Fig. 1 for a representative case in Schwarzschild spacetime for eccentricity $e = 0.5$. The figure shows the angular momentum and energy fluxes (middle and right panels) computed along a portion of the geodesic trajectory (left panel). The QC prescription (blue line) is the least accurate, as *a priori* expected. The QC2PN of Ref. [19]

is more reliable than the QC prescription, though differences up to several percent with respect to numerical data are found. The NCN prescription performs best in reproducing the numerical results; this is a feature of almost all the cases analyzed in this work. To be more quantitative, we considered the analytical/numerical relative differences between orbital-averaged fluxes. For the NCN angular momentum fluxes we get 0.6%, for the QC2PN fluxes we obtain 9.8%, and 14.5% for the QC. For the energy fluxes the hierarchy is the same and we get 0.8%, 18.1%, and 33.4%, respectively. At lower eccentricities, the discrepancies between analytical expressions are milder, while for higher eccentricities the differences are more evident. In particular, for high eccentricity the QC and QC2PN prescriptions exhibit differences up to a factor 2 with the numerical results at apastron. The effects on the dynamics, and thus on the waveform, of using different radiation reactions can be seen for a representative case in Fig. 2. As usual, we adopt Regge-Wheeler-Zerilli normalized multipolar waveforms $\Psi_{\ell m} = h_{\ell m} / \sqrt{(\ell+2)(\ell+1)\ell(\ell-1)}$ where the strain multipoles are defined as

$$h_+ - ih_\times = \frac{1}{D_L} \sum_{\ell=2}^{\infty} \sum_{m=-\ell}^{\ell} h_{\ell m - 2} Y_{\ell m}, \quad (1)$$

where D_L is the luminosity distance and $_{-2}Y_{\ell m}$ are the $s = -2$ spin-weighted spherical harmonics. In the top panel of Fig. 2, we contrast the real part of the $\ell = m = 2$ waveform obtained with the dynamics driven by the NCN radiation reaction (red) with that obtained with the QC prescription (blue). The bottom panel of the figure displays the instantaneous gravitational wave frequency, defined as $\omega_{22} = \dot{\phi}_{22}$ from the amplitude and phase decomposition of the waveform $\Psi_{22} = A_{22} \exp(-i\phi_{22})$. The effects of the different radiation reaction start to be evident after 6-7 orbits, with the QC flux, which is large at the apastron, that progressively circularizes the orbits more and eventually drives a faster transition from inspiral to plunge and merger. The stronger circularization effect of the QC flux is visualized by the frequency evolution in the bottom panel of Fig. 2, with the amplitude of the QC oscillation that is getting progressively smaller than the NCN one. We will see that in the comparable-mass case the action of the radiation reaction on the dynamics is stronger and thus the discrepancies can show up already on a shorter and less eccentric inspiral, as discussed in Sec. V.

The reminder of the paper is structured as follows. In Sec. II we recall the main elements of the EOB model and write explicitly the test-particle limit. Section III describes in detail the different analytical prescriptions used in current EOB models that are finally tested in Sec. IV in the test-mass limit. Section V studies the effects of using different radiation reactions in the comparable-mass case. Finally, in Sec. VI we present a new Newtonian-factorized radiation reaction with 2PN noncircular corrections. Note that a more detailed discussion of the

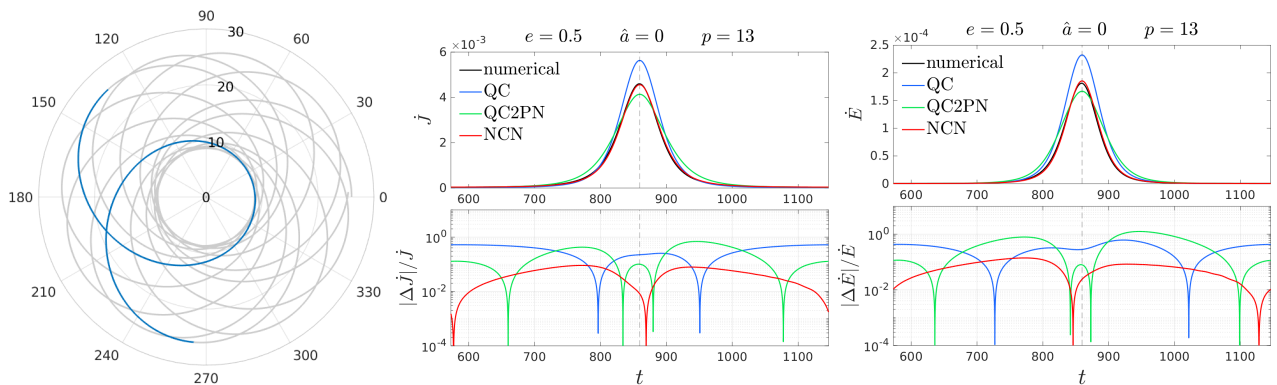


FIG. 1. Test particle orbiting around a Schwarzschild black hole ($\hat{a} = 0$) on a geodesic with eccentricity $e = 0.5$ and semilatus rectum $p = 13$. One radial period is highlighted on the trajectory (left panel) and we show the corresponding fluxes. We contrast the numerical fluxes (black) and the three different analytical fluxes considered in this work: (i) the NCN flux (red), as used in **TEOBResumS**, obtained from Eqs. (16) and (19); (ii) the QC flux (blue) computed from Eq. (21), which is a proxy of the fluxes of **SEOBNRv4EHM** [20]; and (iii) the QC2PN flux (green) computed using Eqs. (22) as taken from Khalil *et al.* [19]. The analytical/numerical relative differences are shown in the bottom panels. The NCN analytical fluxes deliver the closer agreement with the numerical ones either at apastron and periastron. See Sec. III and IV for full discussion.

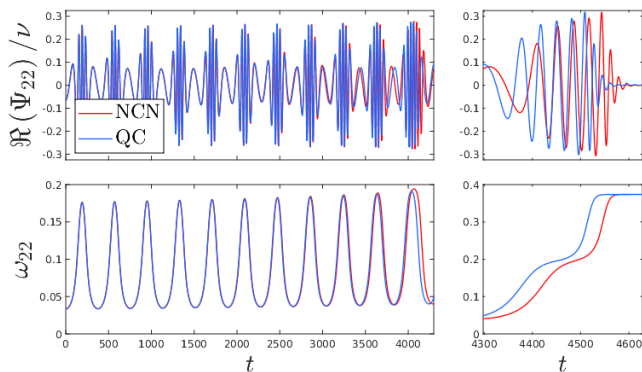


FIG. 2. EOB $\ell = m = 2$ Regge-Wheeler-Zerilli normalized strain waveforms of a test-particle inspiraling and plunging around a Schwarzschild black hole. Initial eccentricity e_0 and semilatus rectum p_0 are $(e_0, p_0) = (0.5, 7.6)$. The inspiral behind the red waveform is driven by the NCN flux, while that of the blue one by the QC flux. In the bottom panels we show the corresponding quadrupolar frequencies. The fact that the QC flux overestimates the correct answer (see Fig. 1) at periastron yields an *unphysical* acceleration of the inspiral related to the (small but non-negligible) circularization of the orbit.

topics presented in Sec. II can be found in Ref. [14].

Throughout this paper, we use geometrized units $G = c = 1$, even if sometimes we will write c explicitly to highlight the PN orders. Moreover, the time and the phase-space variables used in this work are related to the physical ones by $t = T/(GM)$, $r = R/(GM)$, $p_r = P_R/\mu$ and $p_\varphi = P_\varphi/(\mu GM)$, where M is the total mass of the system and μ its reduced mass.

II. EOB DYNAMICS AND TEST-MASS LIMIT

The EOB model maps the relative motion of two bodies with masses m_1 and m_2 into the motion of an effective body into an effective metric that is a continuous ν -deformation of the Kerr metric, with $\nu \equiv m_1 m_2 / (m_1 + m_2)$ being the symmetric mass ratio. Setting $\nu = 0$ we recover the Kerr metric and therefore we describe the motion of a test particle with mass $\mu = \nu M$ in Kerr spacetime, where M is the mass of the Kerr black hole. The EOB model is based on three building blocks: (i) the EOB Hamiltonian \hat{H}_{EOB} [46, 47] that describes the conservative part of the dynamics; (ii) a radiation reaction that consists in an azimuthal and a radial component ($\mathcal{F}_\varphi, \mathcal{F}_r$) and accounts for the loss of energy and angular momentum due to the emission of GWs; (iii) a prescription for the multipolar waveform $h_{\ell m}$ at infinity. Since the description of comparable-mass binaries within the EOB framework is continuously connected to the motion of a test particle by the symmetric mass ratio ν , any analytical structure of the model must be robust and accurate in the test particle limit. Seen the other way around, the test particle limit is a useful *laboratory* to learn and develop new ideas, as originally advocated for in seminal EOB works [27, 48, 49].

Here we consider eccentric (and hyperbolic) equatorial orbits of a test particle around a Kerr black hole with dimensionless spin parameter \hat{a} . Dynamics of this kind have been already discussed in Sec. IIA of Ref. [14] to validate the NCN radiation reaction, but we report here a brief summary for completeness. The equatorial dynamics is obtained solving Hamilton's equations

$$\dot{r} = \left(\frac{A}{B}\right)^{1/2} \frac{\partial \hat{H}_{\text{Kerr}}^{\text{eq}}}{\partial p_{r*}}, \quad (2)$$

$$\dot{\varphi} = \frac{\partial \hat{H}_{\text{Kerr}}^{\text{eq}}}{\partial p_{\varphi}} \equiv \Omega, \quad (3)$$

$$\dot{p}_{r_*} = \left(\frac{A}{B}\right)^{1/2} \left(\hat{\mathcal{F}}_r - \frac{\partial \hat{H}_{\text{Kerr}}^{\text{eq}}}{\partial r} \right), \quad (4)$$

$$\dot{p}_{\varphi} = \hat{\mathcal{F}}_{\varphi}, \quad (5)$$

where $\hat{\mathcal{F}}_{r,\varphi} = \mathcal{F}_{r,\varphi}/\nu$ and $\hat{H}_{\text{Kerr}}^{\text{eq}}$ is the equatorial μ -normalized Kerr Hamiltonian

$$\hat{H}_{\text{Kerr}}^{\text{eq}} = \frac{2\hat{a}p_{\varphi}}{rr_c^2} + \sqrt{A(r) \left(1 + \frac{p_{\varphi}^2}{r_c^2}\right) + p_{r_*}^2} \quad (6)$$

written in terms of the gauge-invariant centrifugal radius r_c [46]

$$r_c^2 = r^2 + \hat{a}^2 + \frac{2\hat{a}^2}{r}, \quad (7)$$

where \hat{a} is the dimensionless Kerr spin parameter.

The metric functions $A(r)$ and $B(r)$ are

$$A(r) = \frac{1 + 2u_c}{1 + 2u} (1 - 2u_c), \quad (8)$$

$$B(r) = \frac{1}{1 - 2u + \hat{a}^2 u^2}, \quad (9)$$

where we used $u = 1/r$ and $u_c = 1/r_c$. In addition, p_{r_*} is the momentum conjugate to the tortoise coordinate r_* , defined as $p_{r_*} = \sqrt{A/B} p_r$. Orbits are characterized using the eccentricity e and the semilatus rectum p , whose definitions are given in terms of the apastron r_+ and the periastron r_- as

$$e = \frac{r_+ - r_-}{r_+ + r_-}, \quad p = \frac{2r_+ r_-}{r_+ + r_-}. \quad (10)$$

For stable orbits, p must satisfy the condition $p > p_s(e, \hat{a})$ where $p_s(e, \hat{a})$ is the separatrix given by a root of [50, 51]

$$p_s^2(p_s - 6 - 2e)^2 + \hat{a}^4(e - 3)^2(e + 1)^2 - 2\hat{a}^2(1 + e)p_s[14 + 2e^2 + p_s(3 - e)] = 0. \quad (11)$$

Geodesics correspond to $\hat{\mathcal{F}}_{\varphi} = \hat{\mathcal{F}}_r = 0$ and e, p are constants of motion. Note that e and p are defined only for bound motion; therefore, eccentricity and semilatus rectum are not defined for hyperbolic configurations. In that case, we use the energy and the angular momentum to characterize the orbits.

III. EOB RADIATION REACTION

In this section we recall the prescriptions for the radiation reaction forces ($\hat{\mathcal{F}}_{\varphi}, \hat{\mathcal{F}}_r$) that are currently used in the **TEOBResumS** model (NCN) [12, 13, 21], in the **SEOBNRv4EHM** [20] model (QC) and proposed, but not implemented yet, in Ref. [19] (QC2PN).

A. Noncircular Newtonian prefactor (TEOBResumS)

The comprehensive work of Ref. [14] clearly indicates that, among various analytical possibilities, incorporating noncircular effects in the radiation reaction via the Newtonian correction factor to the quadrupolar flux mode already yields an excellent agreement ($\sim 1\%$) with the numerical fluxes up to mild values of the eccentricity. Before discussing it explicitly, let us recall its structure for quasicircular orbits. In this case the radial component can be set to zero since $\hat{\mathcal{F}}_r = 0$, as this is equivalent to a gauge choice [23]. Therefore, we have only the angular component,

$$\hat{\mathcal{F}}_{\varphi} = -\frac{32}{5} \nu r_{\Omega}^4 \Omega^5 \hat{f}, \quad (12)$$

where $r_{\Omega} = r \left(1 + \hat{a}r^{-3/2}\right)^{2/3}$ and \hat{f} is the Newton-normalized flux that includes all the (resummed) PN corrections and reads

$$\hat{f} = \sum_{\ell=2}^8 \sum_{m=1}^{\ell} (F_{22}^N)^{-1} F_{\ell m} = \sum_{\ell=2}^8 \sum_{m=1}^{\ell} \hat{F}_{\ell m}. \quad (13)$$

The flux contributions $\hat{F}_{\ell m}$ are written in terms of the multipolar waveform $h_{\ell m}$ and the variable $x = v_{\varphi}^2 = r_{\Omega}^2 \Omega^2$:

$$F_{\ell m} = \frac{1}{8\pi} m^2 \Omega^2 |h_{\ell m}(x)|^2, \quad (14)$$

$$F_{22}^N = \frac{32}{5} x^5. \quad (15)$$

The $h_{\ell m}$ multipoles are factorized and resummed building upon the original prescription of Ref. [27]. Here we use the latest development of resummed circular flux in the test particle limit as discussed in Ref. [14], which yields considerable improvements with respect to previous implementations. In particular, (i) it includes (relative) 6PN orbital information in all multipoles up to $\ell = 8$ included and (ii) the residual amplitude corrections are resummed following the approach of Refs. [37, 38], that is based on the separate treatment of the orbital and spin dependent terms. The accuracy of our circular analytical flux with respect to numerical data is recalled in Appendix A. It must be emphasized that this specific flux is slightly different with respect to the test particle limit of the **TEOBResumS** flux [28], e.g. in the treatment of the $\ell = m = 2$ mode and in the modes with $\ell > 6$. These differences are, however, irrelevant for our current purposes.

The angular component of the generic radiation reaction used in **TEOBResumS** [10, 13, 21] for noncircular binaries is obtained dressing the quadrupolar contribution in $\hat{\mathcal{F}}_{\varphi}^{\text{QC}}$ with the corresponding Newtonian noncircular correction [9], explicitly

$$\hat{\mathcal{F}}_{\varphi}^{\text{NCN}} = -\frac{32}{5} \nu r_{\Omega}^4 \Omega^5 \hat{f}_{\text{nc}22}, \quad (16)$$

where $\hat{f}_{\text{nc}22}$ contains the noncircular corrections $\hat{f}_{\varphi,22}^{\text{Nnc}}$:

$$\hat{f}_{\text{nc}22} \equiv \hat{F}_{22}\hat{f}_{\varphi,22}^{\text{Nnc}} + \hat{F}_{21} + \sum_{\ell \geq 3} \sum_{m=1}^{\ell} \hat{F}_{\ell m}, \quad (17)$$

$$\begin{aligned} \hat{f}_{\varphi,22}^{\text{Nnc}} = & 1 + \frac{3\dot{r}^4}{4r^4\Omega^4} + \frac{3\dot{r}^3\dot{\Omega}}{4r^3\Omega^5} + \frac{3\ddot{r}^2}{4r^2\Omega^4} + \frac{3\ddot{r}\dot{\Omega}}{8r^2\Omega^5} \\ & - \frac{r^{(3)}\dot{r}}{2r^2\Omega^4} + \frac{\dot{r}^2\ddot{\Omega}}{8r^2\Omega^5} + \frac{4\dot{r}^2}{r^2\Omega^2} + \frac{\ddot{r}\ddot{\Omega}}{8r\Omega^5} \\ & - \frac{2\ddot{r}}{r\Omega^2} - \frac{r^{(3)}\dot{\Omega}}{8r\Omega^5} + \frac{3\dot{r}\dot{\Omega}}{r\Omega^3} + \frac{3\dot{\Omega}^2}{4\Omega^4} - \frac{\ddot{\Omega}}{4\Omega^3}. \end{aligned} \quad (18)$$

For the radial component of the radiation reaction $\hat{\mathcal{F}}_r$ we adopt the Padé resummed expression of Refs. [9, 12] that relies on the 2PN-accurate results of Ref. [52],

$$\hat{\mathcal{F}}_r^{\text{NCN}} = \frac{32}{3}\nu \frac{p_{r*}}{r^4} P_2^0[\hat{f}_r^{\text{N}} + \hat{f}_r^{\text{1PN}} + \hat{f}_r^{\text{2PN}}], \quad (19)$$

where

$$\hat{f}_r^{\text{N}} = -\frac{8}{15} + \frac{56}{5}\frac{p_{\varphi}^2}{r}, \quad (20a)$$

$$\begin{aligned} \hat{f}_r^{\text{1PN}} = & -\frac{1228}{105}p_{r*}^2 - \frac{1984}{105}\frac{1}{r} - \frac{124}{105}\frac{p_{r*}^2 p_{\varphi}^2}{r} + \\ & + \frac{1252}{105}\frac{p_{\varphi}^4}{r^3} - \frac{1696}{35}\frac{p_{\varphi}^2}{r^2}, \end{aligned} \quad (20b)$$

$$\begin{aligned} \hat{f}_r^{\text{2PN}} = & \frac{323}{315}p_{r*}^4 + \frac{59554}{2835}r^2 - \frac{1774}{21}\frac{p_{r*}^2 p_{\varphi}^2}{r^2} + \\ & - \frac{628}{105}\frac{p_{r*}^2 p_{\varphi}^4}{r^3} - \frac{29438}{315}\frac{p_{\varphi}^2}{r^3} - \frac{461}{315}\frac{p_{r*}^4 p_{\varphi}^2}{r} + \\ & + \frac{20666}{315}\frac{p_{r*}^2}{r} - \frac{3229}{315}\frac{p_{\varphi}^6}{r^5} - \frac{35209}{315}\frac{p_{\varphi}^4}{r^4}. \end{aligned} \quad (20c)$$

Before applying a Padé approximant is useful to factorize the leading-order term, so that Eq. (19) actually reads $\hat{\mathcal{F}}_r^{\text{NCN}} = \frac{32}{3}\nu \frac{p_{r*}}{r^4} \hat{f}_r^{\text{N}} P_2^0[1 + \hat{f}_r^{\text{1PN}}/\hat{f}_r^{\text{N}} + \hat{f}_r^{\text{2PN}}/\hat{f}_r^{\text{N}}]$.

B. Quasicircular with $\hat{\mathcal{F}}_r \neq 0$ (SEOBNRv4EHM)

Let us move now to describing the QC choice, which mimics what it is implemented in SEOBNRv4EHM [20]. While in TEoBResumS the radial component of the radiation reaction is set to zero for the quasicircular inspiral, it is not the case for SEOBNRv4EHM that has

$$\hat{\mathcal{F}}_{\varphi}^{\text{QC}} = -\frac{32}{5}\nu r_{\Omega}^4 \Omega^5 \hat{f}, \quad (21a)$$

$$\hat{\mathcal{F}}_r^{\text{QC}} = \hat{\mathcal{F}}_{\varphi}^{\text{QC}} \frac{p_r}{p_{\varphi}}. \quad (21b)$$

As mentioned in the Introduction, this quasicircular radiation is also used in SEOBNRv4EHM [20], the eccentric extension of SEOBNRv4HM. We note, however, two aspects. The first one is that Refs. [19, 20] (and not even Refs. [44, 45], which define the SEOBNRv4HM model) do

not write explicitly the leading-order (Newtonian) contribution to $\hat{\mathcal{F}}_{\varphi}$. In particular it is not stated explicitly whether Kepler's constraint is relaxed as originally proposed in Refs. [48] to have a more faithful representation of the angular momentum losses during the plunge. This may induce the reader to think that the dominant term of the angular component is $\hat{\mathcal{F}}_{\varphi}^{\text{qc,LO}} = -32/5\nu\Omega^{7/3}$. Nonetheless, inspecting the public code it is possible to see that also in the SEOBNRv4HM models the Keplerian constraint is relaxed so that $\hat{\mathcal{F}}_{\varphi}^{\text{qc,LO}} = -32/5\nu r_{\Omega}^4 \Omega^5$, as in TEoBResumS. The second aspect to consider is that, consistently with what we wrote in Sec. III A concerning the circular flux, through this paper we will consider \hat{f} as implemented in the test-mass version of TEoBResumS. While the term is formally the same of SEOBNRv4HM, there are some differences in PN orders adopted and in the related resummations that enter \hat{f} and follow Refs. [14, 37, 38]. However, the reliability of the term \hat{f} that we will use in this work is shown in Appendix A. With the aforementioned caveats, the radiation reaction of Eq. (21) is a proxy of the one used in the actual SEOBNRv4EHM model.

C. Quasicircular with 2PN noncircular corrections

Let us finally turn to the QC2PN radiation reaction, that contains 2PN noncircular correction in factorized form as introduced by Khalil *et al.* [19]. The radiation reaction forces are factorized in quasicircular and eccentric parts:

$$\hat{\mathcal{F}}_{\varphi}^{\text{QC2PN}} = \hat{\mathcal{F}}_{\varphi}^{\text{QC}} \hat{\mathcal{F}}_{\varphi}^{\text{ecc}}, \quad (22a)$$

$$\hat{\mathcal{F}}_r^{\text{QC2PN}} = \hat{\mathcal{F}}_r^{\text{QC}} \hat{\mathcal{F}}_r^{\text{ecc}}, \quad (22b)$$

where $\hat{\mathcal{F}}_{\varphi}^{\text{QC}}$ and $\hat{\mathcal{F}}_r^{\text{QC}}$ are the quasicircular terms of Eq. (21), while $\hat{\mathcal{F}}_{\varphi}^{\text{ecc}}$ and $\hat{\mathcal{F}}_r^{\text{ecc}}$ are the noncircular corrections up to 2PN and reduce to unity in the circular case. Their explicit expressions in the test-mass limit, written in terms of (r, p_r, \dot{p}_r) , are reported in Appendix B.

IV. TESTING THE RELIABILITY OF THE EOB RADIATION REACTION

In this section we test the reliability of the radiation reactions discussed in Sec. III comparing the corresponding fluxes with numerical results.

A. Method

The method we use is discussed in Ref. [14], but we report here the main idea since it is crucial for this paper. First, we consider geodesic orbits, so that the radiation reaction does not influence the dynamics. Then, from a given dynamics one computes the energy and angular

momentum analytical fluxes at infinity, \dot{E} and \dot{J} , using the balance equations [52]

$$\dot{E} = -\dot{r}\mathcal{F}_r - \Omega\mathcal{F}_\varphi - \dot{E}_{\text{Schott}}, \quad (23a)$$

$$\dot{J} = -\mathcal{F}_\varphi, \quad (23b)$$

where \dot{E}_{Schott} is the time derivative of the Schott energy. The latter is linked to the interaction of the source with the local field [52]. Following Ref. [9], the Schott energy is factorized in a circular (c) and noncircular (nc) contribution and each term is additionally resummed, yielding

$$E_{\text{Schott}} = \frac{16}{5} \frac{p_{r*}}{r^3} P_2^0[E_{\text{Schott}}^c] P_2^0[E_{\text{Schott}}^{\text{nc}}], \quad (24)$$

where the circular and noncircular parts are at 2PN accuracy and P_2^0 is the (0, 2) Padé approximant. The two contributions explicitly read

$$E_{\text{Schott}}^c = 1 - \frac{157}{56} \frac{1}{r} - \frac{3421}{756} \frac{1}{r^2}, \quad (25)$$

$$\begin{aligned} E_{\text{Schott}}^{\text{nc}} = & \frac{p_\varphi^2}{r} - \frac{3}{2} p_{r*}^2 + \frac{2}{21} \frac{1}{r} - \frac{1}{2} \frac{p_{r*}^2 p_\varphi^2}{r} \\ & + \frac{55}{168} \frac{p_\varphi^4}{r^3} - \frac{575}{168} \frac{p_\varphi^2}{r^2} + \frac{5}{8} p_{r*}^4 \\ & - \frac{2143}{5292} \frac{1}{r^2} - \frac{61}{48} \frac{p_{r*}^2 p_\varphi^2}{r^2} - \frac{13}{168} \frac{p_{r*}^2 p_\varphi^4}{r^3} \\ & + \frac{370189}{84672} \frac{p_\varphi^2}{r^3} + \frac{3}{8} \frac{p_{r*}^4 p_\varphi^2}{r} - \frac{181}{112} \frac{p_{r*}^2}{r} \\ & - \frac{25}{504} \frac{p_\varphi^6}{r^5} - \frac{130223}{28224} \frac{p_\varphi^4}{r^4}. \end{aligned} \quad (26)$$

The analogous contribution to the angular momentum, \dot{J}_{Schott} , can be eliminated with a suitable gauge choice [52]. Given an analytical prescription for the radiation reaction, we compute the analytical fluxes at infinity (\dot{E}, \dot{J}) and compare them with the corresponding numerical results.

B. Numerical fluxes

We use numerical multipolar waveforms at *null-infinity* $h_{\ell m}^{\text{teuk}}$ obtained solving the 2+1 Teukolsky equation [53, 54] with the hyperboloidal time-domain code **Teukode** [42]. Explicitly, the numerical fluxes are given by

$$\dot{E}_{\text{teuk}} = \frac{1}{16\pi} \sum_{\ell=2}^8 \sum_{m=-\ell}^{\ell} |\dot{h}_{\ell m}^{\text{teuk}}|^2, \quad (27a)$$

$$\dot{J}_{\text{teuk}} = -\frac{1}{16\pi} \sum_{\ell=2}^8 \sum_{m=-\ell}^{\ell} m \Im \left(\dot{h}_{\ell m}^{\text{teuk}} \left(\dot{h}_{\ell m}^{\text{teuk}} \right)^* \right). \quad (27b)$$

We use the same geodesic numerical simulations presented in Ref. [14]; therefore, we consider spins in the range $\hat{a} \in [-0.9, 0.9]$ and eccentricities up to $e = 0.9$. For

each pair (e, \hat{a}) we compute the semilatus rectum p according to the separatrix $p_s(e, \hat{a})$. More precisely, we consider *intermediate* and *distant* configurations that have semilatus rectum $p = p_{\text{schw}} p_s(e, \hat{a}) / p_s(e, 0)$, where p_{schw} is 9 and 13, respectively. In Ref. [14] we considered also *near* simulations that had $p(e, \hat{a}) = p_s(e, \hat{a}) + 0.01$; however, we will not consider them in this work since they show a strong zoom-whirl behavior and thus are less significant for testing the noncircular terms. More details on the numerical simulations can be found in Sec. II of Ref. [14].

C. Instantaneous fluxes for eccentric orbits

We start our tests by computing the analytical fluxes along bound geodesics with eccentricities up to $e = 0.9$. We report the trajectories and the instantaneous fluxes for some significant nonspinning cases in Fig. 3, while in Fig. 4 we show some spinning configurations. For each configuration we show the numerical fluxes (black), the NCNfluxes (red) computed using the radiation reaction of Eqs. (16) and (19), the QCfluxes (blue) computed using Eq. (21), and the QC2PN fluxes (green). Figure 3 illustrates that the QC fluxes are the less accurate ones even for $e = 0.1$. The discrepancies with the numerical results are more relevant for higher eccentricities. In particular, the QC fluxes overestimate the numerical flux at periastron in almost all the cases. However, for some cases with high eccentricity and high spin, the QC expressions incidentally provide the best approximation to the numerical fluxes at periastron, as shown in the case with $(e, \hat{a}, p) = (0.7, 0.6, 8.517)$ of Fig. 4. To better understand this aspect, one should note that for high spins (and high eccentricity) the periastron of the orbit is located in stronger field, and thus the numerical fluxes have general-relativistic contributions that are not included in the EOB analytical fluxes. Indeed, the last panel of Fig. 4 highlights that the numerical fluxes are not symmetric with respect to the periastron and that there are quasinormal-modes excitations of the Kerr black hole [55–57]. These excitations are responsible for the oscillations in the relative differences after the periastron passage that can be clearly seen in the case with $(e, \hat{a}) = (0.9, 0.9)$ shown in Fig. 4. As a consequence, the analytical flux underestimates the numerical results in strong field, as already observed in Ref. [14]. Therefore considering that (i) the QC fluxes overestimate the numerical fluxes for all the case with mild spins, and (ii) the numerical fluxes at periastron in the strong field regime naturally overestimate analytical fluxes, we have that there must be some configurations for which the quasicircular prescription will provide the best approximation at periastron. However, in all cases with mild or high eccentricity the QC fluxes are not reliable at apastron, leading to comparatively large relative differences. While this is not relevant from a practical point of view since the main contribution of the radiation re-

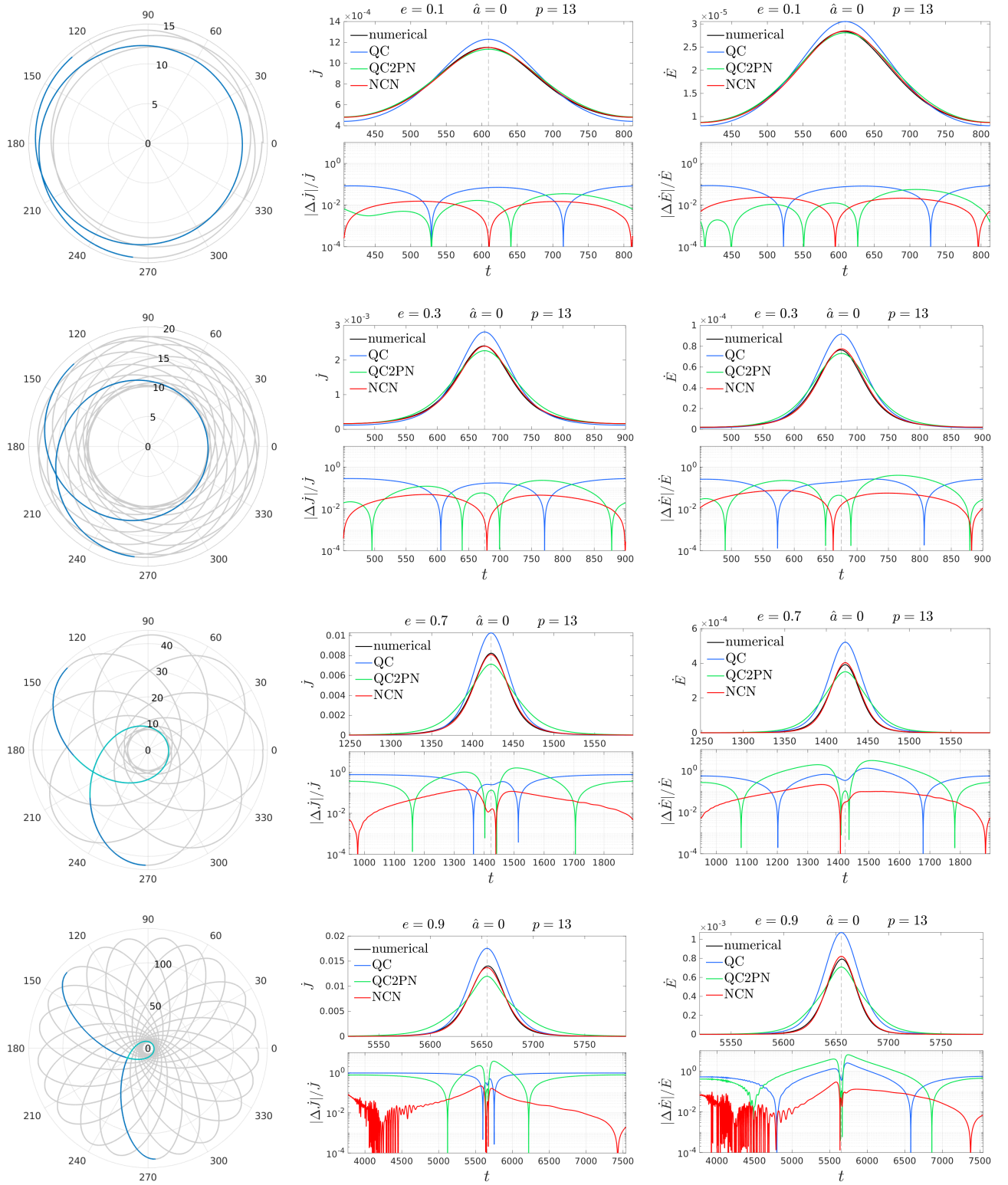


FIG. 3. Geodesic configurations with $\hat{a} = 0$, $p = 13$ and $e = (0.1, 0.3, 0.7, 0.9)$. For each one we show the trajectories highlighting one radial period (blue) and the corresponding fluxes. We contrast the numerical fluxes (black) with the three analytical fluxes considered in this work: the NCN flux (red) computed using Eqs. (16) and (19); the QC flux (blue) from Eq. (21), which is a proxy of the `SEOBNRv4EHM` fluxes, and the QC2PN flux with 2PN noncircular corrections (green) from Eqs. (22). Each subpanel also reports the analytical/numerical relative difference. Note that while the relative differences in the lower panels are always shown over the complete radial period, the fluxes for $e \geq 0.7$ are shown on smaller time intervals (highlighted in aqua-green on the trajectories) in order to better highlight the burst of radiation at periastron passage (marked by a dashed vertical line).

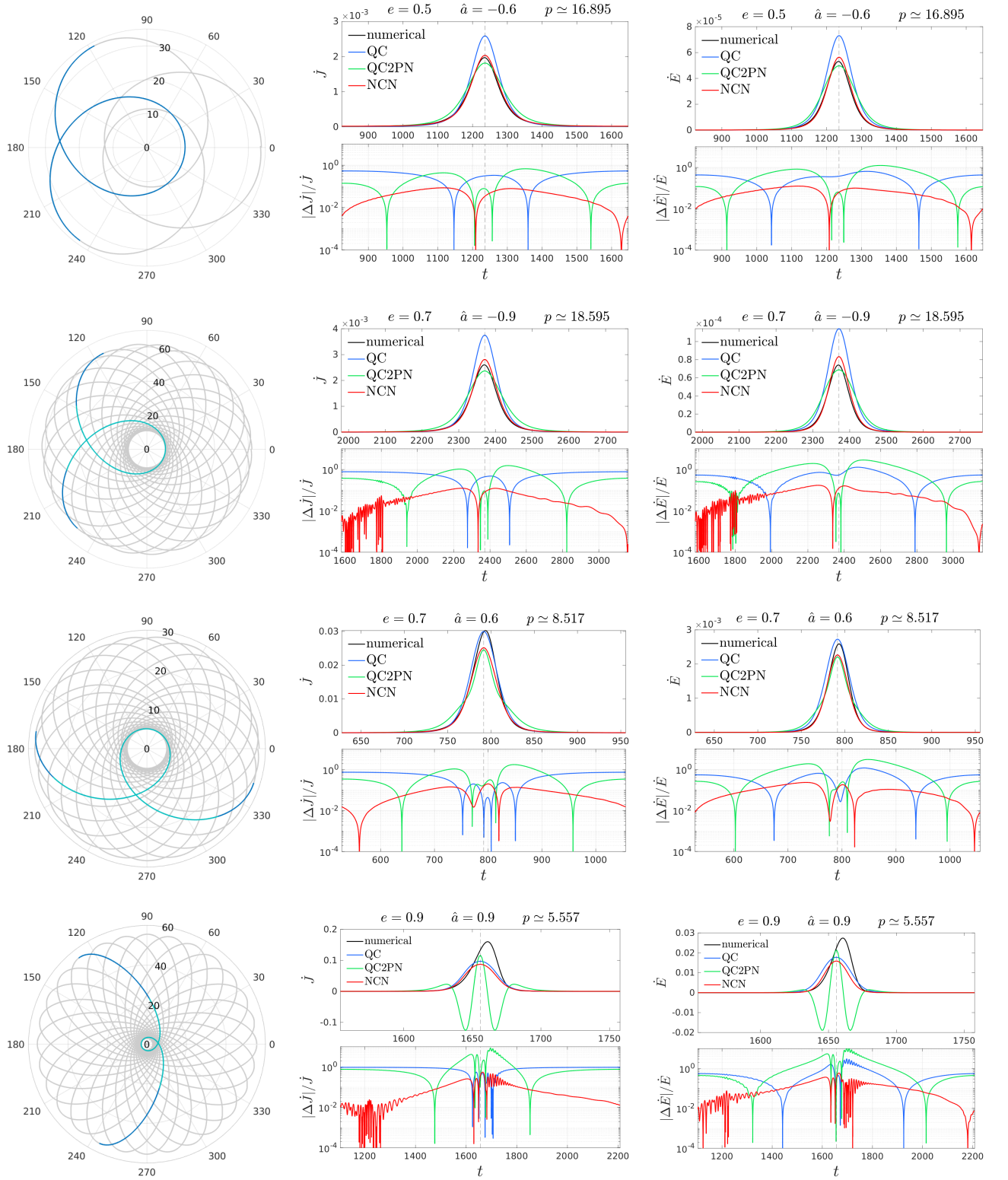


FIG. 4. Analogous to Fig. 3, but for spinning configurations with different eccentricities. The semilata recta are computed according to $p = 13p_s(e, \hat{a})/p_s(e, 0)$. For each configuration we show the trajectories highlighting one radial period (blue) and the corresponding fluxes. We contrast the numerical fluxes (black) with the three analytical fluxes considered in this work: the NCN flux (red) computed using Eqs. (16) and (19); the QC flux (blue) from Eq. (21), which is a proxy of the SEOBNRv4EHM fluxes, and the QC2PN flux with 2PN noncircular corrections (green) from Eqs. (22). Each subpanel also reports the analytical/numerical relative difference. Note that while the relative differences in the lower panels are always shown over the complete radial period, the fluxes for $e \geq 0.7$ are shown on smaller time intervals (highlighted in aqua-green on the trajectories) in order to show better the burst of radiation at the periastron passage (marked by a dashed vertical line).

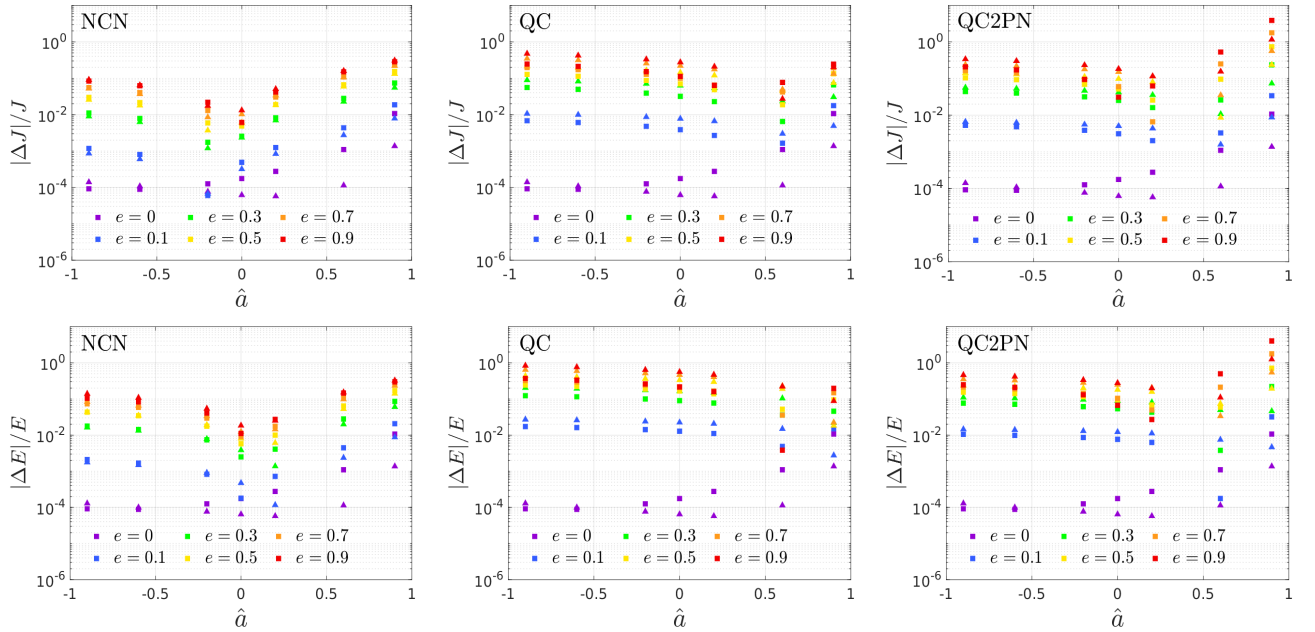


FIG. 5. Analytical/numerical relative differences for the orbital averaged fluxes (angular momentum and energy) that correspond to eccentric configurations. For each configuration the semilatus rectum is computed according to $p = p_{\text{schw}} p_s(e, \hat{a}) / p_s(e, 0)$ where $p_{\text{schw}} = 9$ (squares) or $p_{\text{schw}} = 13$ (triangles).

action to the dynamics happens at periastron, it is, however, an indication that the quasircular prescription is not suited to describe eccentric dynamics, as *a priori* expected. We will further confirm this statement in the next subsection where we will analyze the fluxes more systematically considering the analytical/numerical differences between averaged fluxes over the whole parameter space $(e, \hat{a}) = [0, 0.9] \times [-0.9, 0.9]$. The fact that the QC radiation reaction overestimates the numerical fluxes at periastron generally results in an unphysical acceleration of the dynamics once the corresponding \mathcal{F}_φ enters at the rhs of Hamilton's equations. While an example in the test-mass limit has already been provided in Fig. 2, the relevance of this aspect for comparable-mass binaries will be further discussed in Sec. V.

Let us now focus on the QC2PN prescription, which follows from Ref. [19] (green in Figs. 3 and 4). While for low eccentricity the corresponding fluxes are reliable, as shown in the $e = 0.1$ case of Fig. 4, the prescription starts to be less accurate for mild and high eccentricities. In particular, while this choice is generally more accurate than the QC case at apastron, the relative differences are still larger than the NCN ones. Moreover, when the particle is almost at the periastron or shortly after the periastron passage (i.e. when the radial momentum is close to its maximum value along the orbit), the analytical/numerical relative differences for this prescription reach their maximum and are even larger than for the QC case. This aspect can be clearly seen in all the configurations with $e \geq 0.5$ shown in Figs. 1, 3 and 4. For large values of eccentricity and large spin the fluxes associated to the QC2PN choice can show unphysical be-

haviors, developing multiple peaks and becoming negative. This can be clearly seen in the last configuration of Fig. 4, but we anticipate that a similar pathological behavior can occur even in the nonspinning case if the noncircularity of the orbit is high enough, as shown in the last hyperbolic scattering of Fig. 7 in Sec. IV E. In Fig. 4 we consider configurations with semilatus rectum $p = 13p_s(e, \hat{a})/p_s(e, 0)$, but the pathologic behavior becomes even more relevant if we consider smaller semilatus recta like $p = 9p_s(e, \hat{a})/p_s(e, 0)$.

Let us finally turn to the analysis of the NCN analytical fluxes, repeating for completeness some of the analysis of Ref. [14]. Figure 3 shows that such analytical expressions are the most reliable among the three and this becomes especially evident for $e \geq 0.3$. Note that the NCN expressions are the only ones where the relative differences are smaller at apastron than at periastron, as one would naturally expect since the periastron is reached in a stronger gravitational field, and thus the accuracy of any PN-based expression (though resummed) should be reduced there.

Finally, we conclude with an observation on the numerical fluxes that could be relevant for the next subsection. As can be seen in the last plots of Fig. 3 or in Fig. 4, the relative differences of highly eccentric configuration are noisy for early times (i.e. near the apastron). This is linked to the fact that the numerical flux is still slightly contaminated by the junk radiation¹. However,

¹ The numerical simulations do not start necessarily from $t = 0$.

the highly-eccentric fluxes have a small absolute magnitude near the apastron and thus this contamination does not affect the averaged fluxes that we will consider in the next section. To be more quantitative, consider that for the case with $(e, \hat{a}, p) = (0.9, 0, 13)$ in the last row of Fig. 3 the angular momentum flux and the energy flux have values of $5 \cdot 10^{-8}$ and $2 \cdot 10^{-11}$ at apastron, respectively.

D. Orbital averaged fluxes for eccentric orbits

To have a more systematic picture of the accuracy of the analytical expressions discussed above, it is useful to consider the fluxes averaged along a radial orbit and the corresponding relative differences with the exact quantities. However, this method tests the reliability of the prescriptions in the neighborhood of the periastron, where there is the main contribution to the integrated flux. In other words, with this method it is not possible to see that the QC and QC2PN expressions are not accurate at apastron. We report the analytical/numerical relative differences in absolute value plotted against the Kerr spin parameter \hat{a} in Fig. 5. We use squares as markers to indicate configurations with semilatus rectum $p = 9p_s(e, \hat{a})/p_s(a, 0)$, while we use triangles for $p = 13p_s(e, \hat{a})/p_s(a, 0)$. Note that the results for the NCN were already shown in Ref. [14].

Let us first note in Fig. 5 that the purple markers, corresponding to the circular configurations, are the same in all cases since the circular expressions are shared by the QC, QC2PN and NCN expressions. Their accuracy is further discussed in Appendix A. Already for $e = 0.1$ the three prescriptions provide quite different results: both the QC and QC2PN choices yield significantly larger differences than the NCN one for both energy and angular momentum. This remains true also for larger eccentricities. On the other hand, for spins $\hat{a} \geq 0.6$, the relative differences of the quasicircular prescription are similar to the ones of the **TEOBResumS** fluxes, and even slightly better in some cases. Nonetheless, we have already discussed in Sec. IV C that generally the quasicircular fluxes overestimate the numerical results, but for high spins the numerical fluxes include contributions that are not described by EOB models. For the last prescription shown in Fig. 5, the one that includes 2PN noncircular information, for $\hat{a} \geq 0.6$ we have greater relative differences than for the other two prescriptions, but we already argued that for high spins and/or high eccentricity this prescription shows pathological behavior. For smaller spins instead the analytical/numerical discrepancies are bigger for farther simulations, as happens also for the other radiation reactions independently of the spin considered (with few exceptions). This issue of the QC2PN choice can even lead to negative averaged fluxes; for example, this happens in the configurations with $\hat{a} = 0.9$, $e \geq 0.7$ and $p = 9p_s(e, \hat{a})/p_s(e, 0)$.

Finally, we can consider all the simulations for a certain

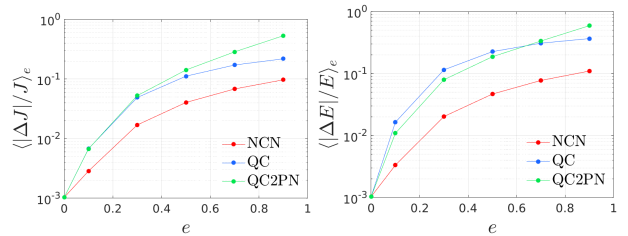


FIG. 6. Means of the analytical/numerical relative differences of the orbital averaged fluxes, graphical representation of Table I. Each point represents the mean of the averaged fluxes of all the configurations with a certain value of eccentricity, that we indicate as $\langle \dots \rangle_e$. Note that we consider $\hat{a} = (0, \pm 0.2, \pm 0.6, \pm 0.9)$ and two semilatus recta for each pair (e, \hat{a}) , so that each point is the mean value over 14 averaged fluxes. As can be seen, NCN is, on average, the most reliable radiation reaction.

TABLE I. Averaged analytical/numerical relative differences $\langle \delta F \rangle = \langle |\Delta F|/F \rangle$ for the fluxes averaged over a radial orbit for the three analytical possibilities, NCN, QC and QC2PN. We consider the means over the simulations with same eccentricity, the average for the nonspinning configurations, and the average for all the configurations. The values are reported in percentage. The relative differences averaged over the circular configurations are $\langle \delta J \rangle_c = \langle \delta E \rangle_c = 0.10\%$. The averages at fixed eccentricity are shown in Fig. 6.

[%]	NCN		QC		QC2PN	
	$\langle \delta J \rangle$	$\langle \delta E \rangle$	$\langle \delta J \rangle$	$\langle \delta E \rangle$	$\langle \delta J \rangle$	$\langle \delta E \rangle$
$e = 0.1$	0.29	0.33	0.68	1.64	0.67	1.09
$e = 0.3$	1.70	2.02	4.89	11.46	5.26	7.93
$e = 0.5$	4.04	4.66	11.15	22.53	14.17	18.65
$e = 0.7$	6.81	7.73	17.17	30.84	28.54	33.47
$e = 0.9$	9.69	10.97	21.80	36.60	53.15	59.08
$\hat{a} = 0$	0.44	0.60	8.60	18.72	5.43	9.49
all	3.77	4.30	9.30	17.20	16.98	20.05

value of eccentricity and we can obtain the mean of the corresponding averaged fluxes. We indicate this averaged at fixed eccentricity as $\langle \dots \rangle_e$. In Fig. 6 we report these averages for the fluxes considered so far, showing once again that the NCN is the most reliable for every value of eccentricity.

To conclude, also the systematic study of the reliability of the three prescriptions considered so far suggests that the standard radiation reaction of **TEOBResumS** is the most accurate, both for low and high eccentricity.

E. Hyperbolic orbits

We now turn our attention to unbound orbits. We consider three hyperbolic geodesic scatterings in Schwarzschild spacetime whose orbits are shown in Fig. 7 together with the corresponding analytical/numerical an-

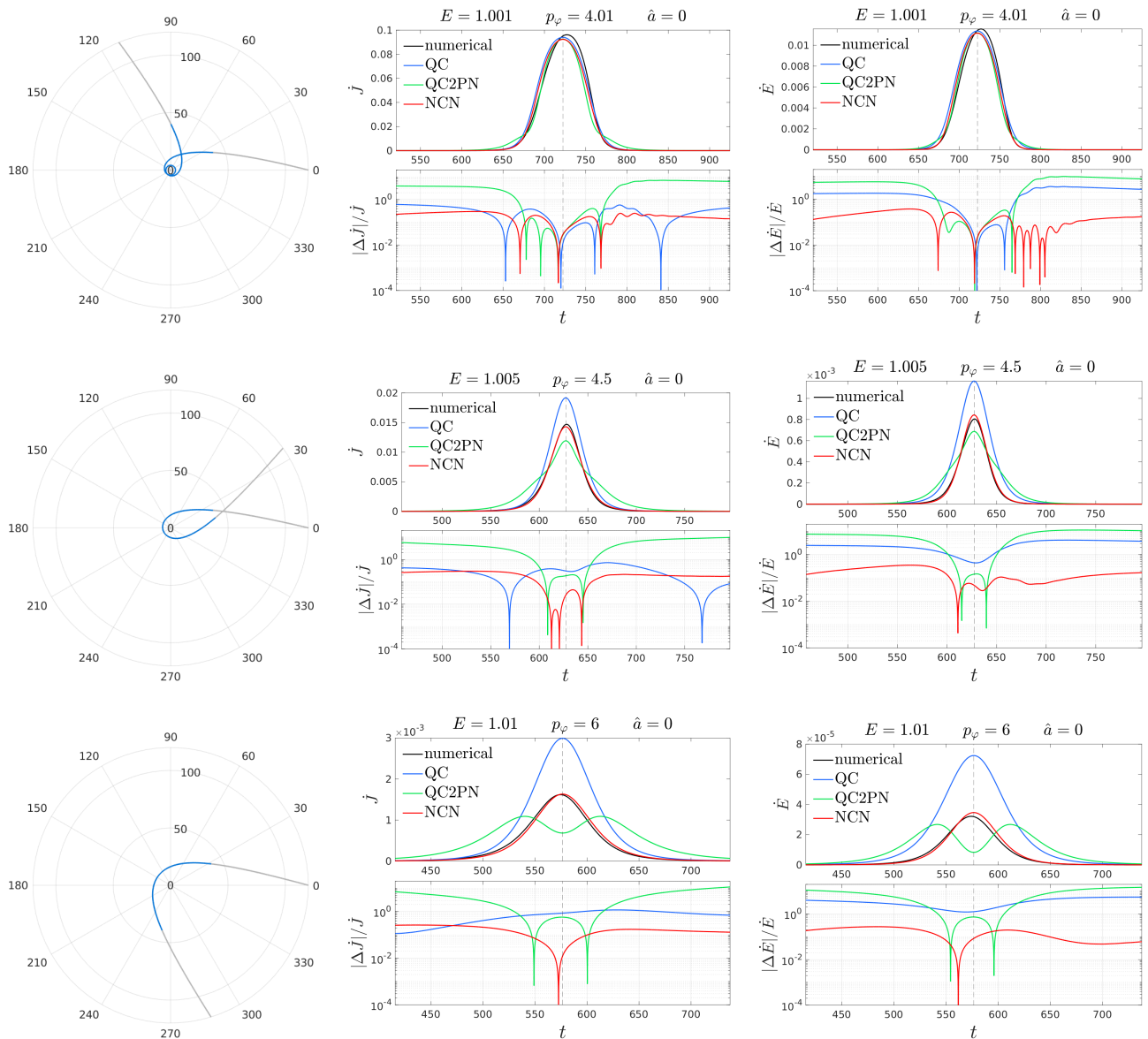


FIG. 7. Hyperbolic geodesics in Schwarzschild spacetime. In the trajectories we highlight in blue the part that corresponds to $r \leq 40$; the fluxes are computed on this interval. We contrast the numerical fluxes (black) with the three analytical fluxes considered in this work: the NCN flux (red) computed using Eqs. (16) and (19); the QC flux (blue) from Eq. (21), that is a proxy of the SEOBNRv4EHM fluxes, and the QC2PN flux with 2PN noncircular corrections (green) from Eqs. (22). Each subpanel also reports the analytical/numerical relative difference. For each analytical flux we also show the relative difference with the numerical result. The dashed vertical line marks the closest passage to the central black hole.

gular momentum and energy fluxes. In all the three cases considered, the initial separation is $r = 120$, but we show only the time interval that corresponds to $r \leq 40$. As already discussed in Sec. II, our definitions of eccentricity and semilatus rectum are not valid for unbound motion; thus, we use the energy E and the angular momentum p_φ , which are constants of motion, to characterize our orbits. The selected values are also reported in Fig. 7 for each case.

The first configuration considered exhibits a strong zoom-whirl behavior. While during the circular whirl at periastron all the three prescriptions provide similar

results, the differences between them are clearly visible in the zoom part. Here, the less reliable prescription is the one using the QC2PN flux, as it gives differences well beyond the 100% either before and after the whirl phase. This issue is even more evident when inspecting the other two configurations, which have larger energies and larger angular momenta. In particular, for $(E, p_\varphi) = (1.01, 6)$ the QC2PN fluxes even develop multiple peaks. The QC fluxes are more solid, but the relative differences with the numerical results are still very large and they always overestimate the numerical results at periastron, especially for the energy fluxes. Finally, the fluxes computed

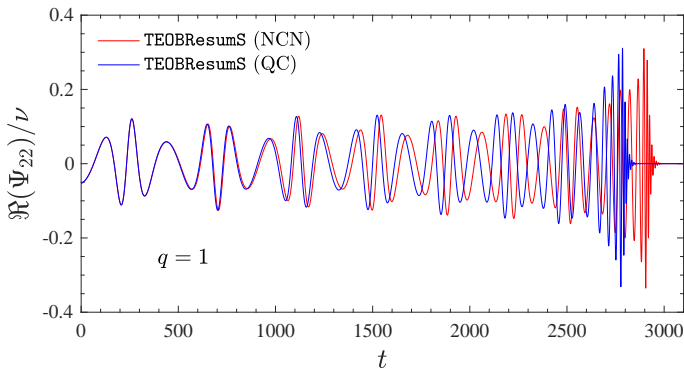


FIG. 8. Equal-mass case ($q = 1$), initial EOB eccentricity ~ 0.2 , **TEOBResumS** [21] evolution: effect of using the circular $\hat{\mathcal{F}}_\varphi$ (QC) instead of the full one (NCN) with the Newtonian noncircular correction. Both dynamics are started with the same initial data. This BBH configuration corresponds to the SXS:BBH:1363 configuration discussed in Table IV of Ref. [21]. The qualitative behavior is analogous to the test-mass case shown in Fig. 2.

using the NCN choice are, once again, the most reliable and robust, showing smaller quantitative discrepancies with the numerical results for all the three configurations considered.

V. COMPARABLE-MASS CASE

We investigate to which extent our findings in the test-mass case carry over to comparable-mass binaries. We concentrate on a single case study of an equal-mass, nonspinning binary black hole (BBH) configuration with initial (nominal) EOB eccentricity ~ 0.2 , and use the SXS:BBH:1363 dataset of the SXS catalog [58]. This is configuration 9 in Table IV of Ref. [21] used in both our previous work and in Ref. [20]. For the details about the setup of initial data, we refer the reader to Refs. [9, 12, 13, 21]

On the EOB side, we consider the latest development of the eccentric version of **TEOBResumS**, as introduced in Ref. [13], since it delivers the highest EOB/NR agreement (including scattering angle measures). The only change with respect to Ref. [13] is that we adopt the 2PN-accurate, factorized and resummed, waveform of Ref. [21]. Using this baseline model, we employ two different radiation reactions: (i) the complete (NCN) version of $\hat{\mathcal{F}}_\varphi$, which includes the leading-order noncircular correction in the $\ell = m = 2$ mode and (ii) the quasicircular (QC) $\hat{\mathcal{F}}_\varphi$ but keeping $\mathcal{F}_r \neq 0$. In both cases, the dynamics starts at the apastron² with the same apastron

frequency, ω_a^{EOB} , and EOB eccentricity at this frequency, $e_{\omega_a}^{\text{EOB}}$, $(e_{\omega_a}^{\text{EOB}}, \omega_a^{\text{EOB}}) = (0.30479, 0.01908)$. Figure 8 compares the two waveforms obtained from the two EOB dynamics. Analogously to the test-mass case of Fig. 2, the QC inspiral is shorter when compared to the NCN because of the larger amount of radiation emitted at each periastron passage. The previous results using the exact test-mass data suggest that the QC acceleration is unphysical. This is key to understand the EOB/NR comparison in the equal-mass case.

An EOB/NR phasing analysis for SXS:BBH:1363 with the **TEOBResumS** NCN radiation reaction was recently considered in Ref. [21] (see Fig. 12 there). This result is reported here in the left panel of Fig. 9 to ease the reader: the agreement is excellent with ~ -0.22 rad accumulated up to merger, a phase difference within the NR uncertainty ($\delta\phi_{\text{mrg}}^{\text{NR}} = 0.58$ rad, see Table IV of [21]). The corresponding EOB/NR maximum unfaithfulness using Advanced LIGO noise was $\bar{F}_{\text{EOB/NR}}^{\text{max}} = 0.25\%$ (see Ref. [21] and Fig. 10 below). The left panel of Fig. 9 highlights that not only is the EOB/NR phase difference rather small (always between $[-0.1, 0.05]$ rad), but it also *decreases with time*, as one is *a priori* expecting from two orbital dynamics that progressively circularize in the same way. An EOB/NR phasing for SXS:BBH:1363 with the QC radiation reaction was also recently reported in [20], using the $\hat{\mathcal{F}}_\varphi$ implementation of **SEOBNRv4EHM**. Although no phase differences are explicitly shown, the authors report EOB/NR unfaithfulness $\sim 0.1\%$. The findings of Ref. [20] seem to suggest that the QC azimuthal force yields a faithful representation of the eccentric inspiral dynamics and waveform, at least for mild eccentricities, comparable to the NCN. This would be in stark contrast with the differences between NCN-QC and NR observed in Fig. 8 and discussed above. We now use the flexibility of **TEOBResumS** to demonstrate that the conclusion is incorrect and, at the same time, to highlight subtle aspects in EOB/NR comparisons using short, eccentric waveforms.

As a first step, we construct an EOB QC model consistent with the main features of **SEOBNRv4EHM**. This is done by: (i) switching off the noncircular correction to $\hat{\mathcal{F}}_\varphi$ and (ii) redetermining the effective 5PN parameter a_6^c using the QC flux.³ We consider only the $q = 1$ case, and we find that $a_6^c = -97$ (instead of $a_6^c = -93.0366$, Eq. (41) of Ref. [13]) is a good choice for our purposes. In the second step, we proceed with EOB/NR phasing with this *flexed* QC model. Following Ref. [13] we retune the initial dynamical parameters $(e_{\omega_a}^{\text{EOB}}, \omega_a^{\text{EOB}})$ to minimize as much as possible the EOB/NR phase difference during the eccentric inspiral⁴.

² See Ref. [20] for an improved initial data setup that, involving the eccentric anomaly, allows to start the dynamics at a different point of the orbit.

³ This step is necessary since the effective 5PN parameter a_6^c was determined in Ref. [13] by comparison with quasicircular NR simulations with the full NCN flux and will impact only the late plunge and merger part of the waveform.

⁴ Differently from Ref. [20] we perform this step manually, by tun-

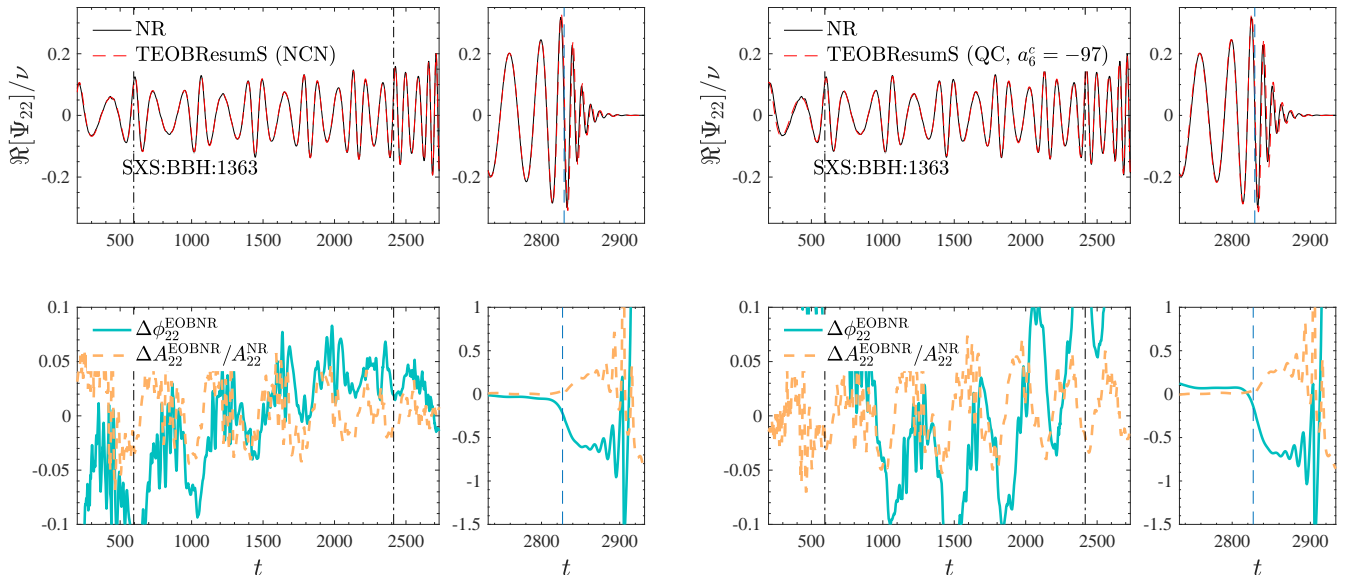


FIG. 9. EOB/NR phasing comparison for SXS:BBH:1363. Left: **TEOBResumS** waveform model of Refs. [13, 21] using the complete NCN expression for $\hat{\mathcal{F}}_\varphi$ with initial parameters $(e_{\omega_a}^{\text{EOB}}, \omega_a^{\text{EOB}}) = (0.30479, 0.01908)$ [see Fig. 12 of [21]]. Right: Modified **TEOBResumS** with the *quasicircular* (QC) $\hat{\mathcal{F}}_\varphi$, without leading noncircular terms, and $a_6^c = -97$. The initial parameters are $(e_{\omega_a}^{\text{EOB}}, \omega_a^{\text{EOB}}) = (0.315, 0.018239)$. The vertical dot-dashed lines indicate the alignment region. On such a short-length waveform the absence of noncircular corrections in $\hat{\mathcal{F}}_\varphi$ can be (partially) reabsorbed in the initial conditions. However, the stronger orbital circularization yielded by the QC model clearly shows up in the last three orbits.

Using $(e_{\omega_a}^{\text{EOB}}, \omega_a^{\text{EOB}}) = (0.30479, 0.01908)$, we obtain an EOB/NR phase difference of ~ -0.14 rad accumulated to merger, as shown in the right panel of Fig. 9. Although less good than for the NCN model, this is a close performance. In summary, this demonstrates that by suitably tuning the initial data parameters it is possible to obtain small phasing errors and faithful waveforms even with a significantly less accurate QC radiation reaction prescription. However, we crucially note that the phase difference is now *increasing with time* in the last few orbits, with a clear quasi-linear trend starting around $t \sim 1500$. This is qualitatively very different from the NCN model, although *globally* the performances of the two waveforms are approximately comparable.

Following Ref. [13], we calculate the EOB/NR unfaithfulness with LIGO noise, and present it in Fig. 10. Although the choice of $(e_{\omega_a}^{\text{EOB}}, \omega_a^{\text{EOB}})$ in the QC model might be further optimized, the NCN model shows better matches than the QC model. It does not seem possible to fully cancel the difference between NCN and QC as the latter is related to the faster circularization of the orbit yielded by the QC flux. This fact is evident from Fig. 11, in which we compare the time evolution of the instantaneous GW frequency of the two models. Even if the NCN

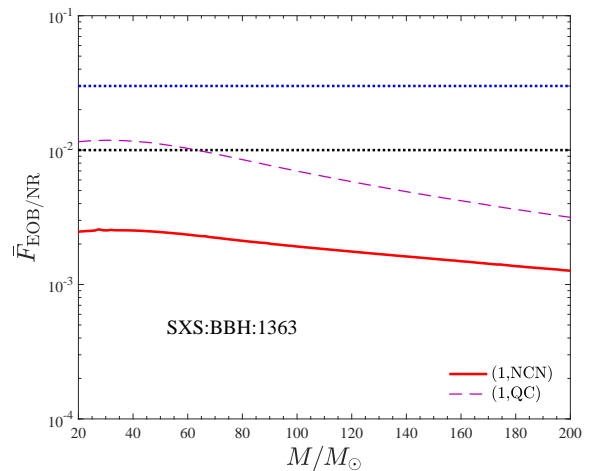


FIG. 10. EOB/NR unfaithfulness computation with the Advanced LIGO noise using the standard NCN **TEOBResumS** model of Ref. [21] or the QC version discussed here. The faster circularization of the QC model results in $\bar{F}_{\text{EOB/NR}}$ slightly above the 1% threshold (see Fig. 11).

and QC choices for $(e_{\omega_a}^{\text{EOB}}, \omega_a^{\text{EOB}})$ give frequency oscillations that are very compatible among themselves and with the NR during the first orbits (say up to $t \sim 1500$ in Fig. 11) the circularization of QC is faster: the amplitude of the frequency oscillation decreases, with fractional difference with NR (bottom panel) that is more than twice larger than the NCN case.

This analysis indicates that the QC expression of $\hat{\mathcal{F}}_\varphi$

ing the parameters iteratively, without any automatized procedure. Note also that Ref. [20] does not look at the phase difference, but at the EOB/NR unfaithfulness, which in our case is checked *a posteriori*. Our results might be improved but are sufficient for our purposes.

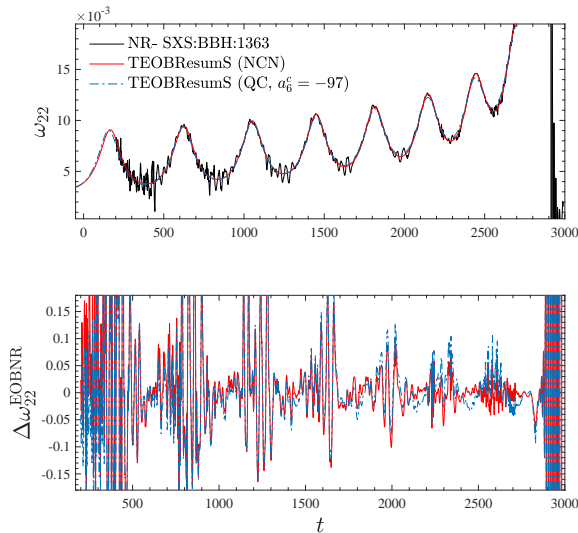


FIG. 11. Time domain frequency evolution. Top panel: comparison between NR and the NCN or QC version of TEOBResumS. Bottom panel: fractional frequency difference with NR. The picture confirms that the NCN and QC initial conditions are approximately coherent among themselves and with the NR curve. The stronger circularization yielded by the QC $\hat{\mathcal{F}}_\varphi$ entails a noticeable EOB/NR disagreement toward the late inspiral.

can introduce large systematics and it is thus *not suited* to construct faithful and robust EOB template waveforms for eccentric binaries. Crucially, standard phasing and faithfulness diagnostic can fail to capture these system-

atic errors, especially if a short NR waveform is employed. The faster circularization of the orbit given by the QC choice can be easily overlooked in the minimization of the initial data parameters thus leading to large phase errors on longer signals.

VI. 2PN CORRECTIONS IN FACTORIZED AND RESUMMED FORM

Reference [21] introduced high PN noncircular terms in the Newtonian-factorized waveform as a multiplicative correction to the generic Newtonian prefactor. After suitable resummations, this yielded an improved analytical/numerical waveform agreement with respect to the use of only the generic Newtonian prefactor, especially for the phase. The aim of this section is to explore the performance of an analogous procedure applied to the flux. For simplicity, and since in any case our $\hat{\mathcal{F}}_\varphi$ is non-circular flexed only in the $\ell = m = 2$ mode, we limit here our analysis only to this mode. A more complete investigation is postponed to future work.

A. 2PN-accurate quadrupolar flux

In Ref. [21] we recovered the full multipolar fluxes at 2PN accuracy in EOB coordinates as a consistency check of our waveform calculation. In particular, starting from the instantaneous part of the waveform we could explicitly recover the 2PN-accurate flux in EOB coordinates as obtained in Ref. [52]. For our current factorization purposes, we show here explicitly the $\ell = m = 2$ flux multipole up to 2PN order, including *both* the instantaneous and tail parts,

$$\begin{aligned}
 F_{22}^{2\text{PN}} = & p_{r*}^2 p_\varphi u^3 - 2p_\varphi^3 u^5 - 2p_\varphi u^4 + \frac{1}{c^2} \left\{ p_\varphi u^5 \left[\frac{689}{42} - \frac{33\nu}{7} + \left(\frac{109}{7} - \frac{61\nu}{7} \right) p_\varphi^2 u + \left(\frac{17}{42} - \frac{12\nu}{7} \right) p_\varphi^4 u^2 \right] \right. \\
 & - p_{r*}^2 p_\varphi u^4 \left[\frac{148}{21} - \frac{36\nu}{7} + p_\varphi^2 u \left(\frac{7}{3} - \frac{21\nu}{2} \right) \right] - p_{r*}^4 p_\varphi u^3 \left(\frac{145}{42} + \frac{9\nu}{14} \right) \left. \right\} + \frac{\pi}{c^3} \left[u^5 \left(\frac{9}{128} - \frac{173p_\varphi^2 u}{10} \right. \right. \\
 & + \frac{79309p_\varphi^4 u^2}{5760} - \frac{889p_\varphi^6 u^3}{32} + \frac{9157p_\varphi^8 u^4}{384} - \frac{697p_\varphi^{10} u^5}{72} + \frac{47p_\varphi^{12} u^6}{640} + \frac{643p_\varphi^{14} u^7}{480} - \frac{97p_\varphi^{16} u^8}{288} \left. \right) \\
 & + p_{r*}^2 u^4 \left(\frac{215}{192} + \frac{91109p_\varphi^2 u}{5760} - \frac{811p_\varphi^4 u^2}{24} + \frac{14659p_\varphi^6 u^3}{192} - \frac{51487p_\varphi^8 u^4}{576} + \frac{22975p_\varphi^{10} u^5}{384} - \frac{3489p_\varphi^{12} u^6}{160} \right. \\
 & + \left. \frac{485p_\varphi^{14} u^7}{144} \right) - p_{r*}^4 u^3 \left(\frac{1219}{1152} - \frac{1471p_\varphi^2 u}{576} + \frac{449p_\varphi^4 u^2}{128} - \frac{3677p_\varphi^6 u^3}{576} + \frac{769p_\varphi^8 u^4}{144} - \frac{49p_\varphi^{10} u^5}{32} \right) \left. \right] \\
 & - \frac{1}{c^4} \left\{ p_\varphi u^6 \left[\frac{8852}{189} - \frac{12335\nu}{378} + \frac{268\nu^2}{27} + p_\varphi^2 u \left(\frac{21001}{882} - \frac{52147\nu}{588} + \frac{7661\nu^2}{294} \right) + p_\varphi^4 u^2 \left(\frac{59}{882} - \frac{60901\nu}{1764} \right. \right. \right. \\
 & + \left. \left. \frac{7663\nu^2}{1764} \right) + p_\varphi^6 u^3 \left(\frac{851}{882} - \frac{4987\nu}{882} - \frac{3295\nu^2}{1764} \right) \right] - p_{r*}^2 p_\varphi u^5 \left[\frac{10277}{882} - \frac{60065\nu}{1764} + \frac{7799\nu^2}{441} \right.
 \end{aligned}$$

$$\begin{aligned}
& + p_\varphi^2 u \left(-\frac{6465}{392} - \frac{48385\nu}{441} + \frac{22237\nu^2}{441} \right) + p_\varphi^4 u^2 \left(\frac{709}{84} - \frac{685\nu}{24} + \frac{463\nu^2}{168} \right) - p_{r_*}^4 p_\varphi u^4 \left[\frac{6527}{441} + \frac{6809\nu}{1764} \right. \\
& \left. - \frac{14921\nu^2}{1764} + p_\varphi^2 u \left(\frac{2923}{588} - \frac{4889\nu}{588} - \frac{6317\nu^2}{294} \right) \right] \Bigg\}, \quad (28)
\end{aligned}$$

where for the sake of simplicity we considered an expansion around 0 of p_{r_*} up to order $\mathcal{O}(p_{r_*}^4)$. For completeness, Appendix C also reports the other flux multipoles relevant at 2PN order.

B. Factorization and resummation

Our aim here is to add 2PN-accurate noncircular corrections to the flux contribution of the mode $\ell = m = 2$. This is achieved by dressing the first term of Eq. (17) with an additional correcting factor $\hat{F}_{\varphi,22}^{2\text{PN}_{\text{nc}}}$ derived from the full noncircular 2PN flux $\hat{F}_{22}^{2\text{PN}}$ written in Eq. (28). Following the same reasoning implemented for the waveform in Ref. [21], the straightforward procedure we use is the following:

- (i) starting from the Taylor expanded flux $F_{22}^{2\text{PN}}$, we factorize the full Newtonian contribution $F_{22}^N \hat{f}_{\varphi,22}^{\text{N}_{\text{nc}}}$, and we use in the latter the 2PN-accurate EOB equations of motion to replace the time derivatives and expand the residual up to $\mathcal{O}(1/c^4)$,
- (ii) we single out the circular part $\hat{F}_{22}^{2\text{PN}_{\text{c}}}$ of the Newtonian-factorized flux by simply taking the limit $p_{r_*} \rightarrow 0$,
- (iii) we factorize the circular part computed in the previous step and compute the desired noncircular correction $\hat{F}_{22}^{2\text{PN}_{\text{nc}}}$.

In formulas we have

$$\hat{F}_{22}^{2\text{PN}_{\text{c}}} \equiv \lim_{p_{r_*} \rightarrow 0} T_{2\text{PN}} \left[\frac{F_{22}^{2\text{PN}}}{\left(F_{22}^N \hat{f}_{\varphi,22}^{\text{N}_{\text{nc}}} \right)_{\text{EOMs}}} \right], \quad (29)$$

$$\hat{F}_{22}^{2\text{PN}_{\text{nc}}} \equiv T_{2\text{PN}} \left[\frac{F_{22}^{2\text{PN}}}{\left(F_{22}^N \hat{f}_{\varphi,22}^{\text{N}_{\text{nc}}} \right)_{\text{EOMs}} \hat{F}_{22}^{2\text{PN}_{\text{c}}}} \right], \quad (30)$$

where the operator $T_{2\text{PN}}$ performs a Taylor expansion up to the 2PN order and the subscript “EOMs” manifests the replacement of the time derivatives in the Newtonian flux with the corresponding EOB equations of motion. The resulting noncircular factor (30) comes out naturally split in an instantaneous and a tail part which appear at different PN orders. For this reason one can readily factorize it further in an instantaneous and a tail factor,

$$\hat{F}_{22}^{2\text{PN}_{\text{nc}}} = \hat{F}_{22}^{2\text{PN}_{\text{nc},\text{inst}}} \hat{F}_{22}^{2\text{PN}_{\text{nc},\text{tail}}}, \quad (31)$$

which explicitly read

$$\begin{aligned}
\hat{F}_{22}^{2\text{PN}_{\text{nc},\text{inst}}} &= 1 + \frac{1}{c^2} \left[\frac{p_{r_*}^2}{(1 + p_\varphi^2 u)^2} \left(\frac{281}{168} + \frac{31\nu}{28} \right) \hat{f}_{p_{r_*}^2}^{1\text{PN}} \right. \\
&+ \left. \frac{p_{r_*}^4}{u(1 + p_\varphi^2 u)^3} \left(\frac{5 - 6\nu}{16} \right) \hat{f}_{p_{r_*}^4}^{1\text{PN}} \right] \quad (32)
\end{aligned}$$

$$\begin{aligned}
&+ \frac{1}{c^4} \left[\frac{p_{r_*}^2 u}{(1 + p_\varphi^2 u)^3} \left(\frac{159697}{42336} - \frac{2081\nu}{10584} + \frac{20345\nu^2}{10584} \right) \hat{f}_{p_{r_*}^2}^{2\text{PN}} \right. \\
&+ \left. \frac{p_{r_*}^4}{p_\varphi(1 + p_\varphi^2 u)^4} \left(\frac{225067}{84672} + \frac{18119\nu}{10584} + \frac{6893\nu^2}{21168} \right) \hat{f}_{p_{r_*}^4}^{2\text{PN}} \right],
\end{aligned}$$

$$\begin{aligned}
\hat{F}_{22}^{2\text{PN}_{\text{nc},\text{tail}}} &= 1 + \frac{\pi}{c^3} \left[-\frac{p_{r_*}^2}{p_\varphi(1 + p_\varphi^2 u)^2} \frac{887}{1536} \hat{t}_{p_{r_*}^2}^{1.5\text{PN}} \right. \\
&+ \left. \frac{p_{r_*}^4}{p_\varphi u(1 + p_\varphi^2 u)^3} \frac{2215}{9216} \hat{t}_{p_{r_*}^4}^{1.5\text{PN}} \right]. \quad (33)
\end{aligned}$$

Again, in the results reported above we expand in p_{r_*} up to order $\mathcal{O}(p_{r_*}^4)$. The terms $\hat{f}_{p_{r_*}^2}^{\text{PN}}$ and $\hat{t}_{p_{r_*}^2}^{1.5\text{PN}}$ are polynomials in the Newtonian-order variable $y = p_\varphi^2 u$. For the instantaneous part the coefficients of the polynomials contain also the symmetric-mass ratio ν and read

$$\hat{f}_{p_{r_*}^2}^{1\text{PN}} = 1 + \frac{2(571 - 54\nu)}{281 + 186\nu} y + \frac{1061 - 390\nu}{281 + 186\nu} y^2, \quad (34)$$

$$\hat{f}_{p_{r_*}^4}^{1\text{PN}} = 1 + \frac{2(395 - 366\nu)}{21(5 - 6\nu)} y + \frac{295 - 234\nu}{7(5 - 6\nu)} y^2, \quad (35)$$

$$\begin{aligned}
\hat{f}_{p_{r_*}^2}^{2\text{PN}} &= 1 + \frac{2(503861 - 236326\nu - 42992\nu^2)}{159697 - 8324\nu + 81380\nu^2} y \\
&+ \frac{6(144635 - 100862\nu - 59260\nu^2)}{159697 - 8324\nu + 81380\nu^2} y^2 \\
&- \frac{6(119807 - 50090\nu + 28256\nu^2)}{159697 - 8324\nu + 81380\nu^2} y^3 \\
&- \frac{21(26487 - 19592\nu + 428\nu^2)}{159697 - 8324\nu + 81380\nu^2} y^4, \quad (36)
\end{aligned}$$

$$\begin{aligned}
\hat{f}_{p_{r_*}^4}^{2\text{PN}} &= 1 + \frac{2(1028891 + 66902\nu - 13616\nu^2)}{225067 + 144952\nu + 27572\nu^2} y \\
&+ \frac{6(670405 + 13630\nu + 8948\nu^2)}{225067 + 144952\nu + 27572\nu^2} y^2 \\
&+ \frac{6(548563 + 5454\nu + 42912\nu^2)}{225067 + 144952\nu + 27572\nu^2} y^3 \\
&+ \frac{3(478421 - 54244\nu + 40444\nu^2)}{225067 + 144952\nu + 27572\nu^2} y^4, \quad (37)
\end{aligned}$$

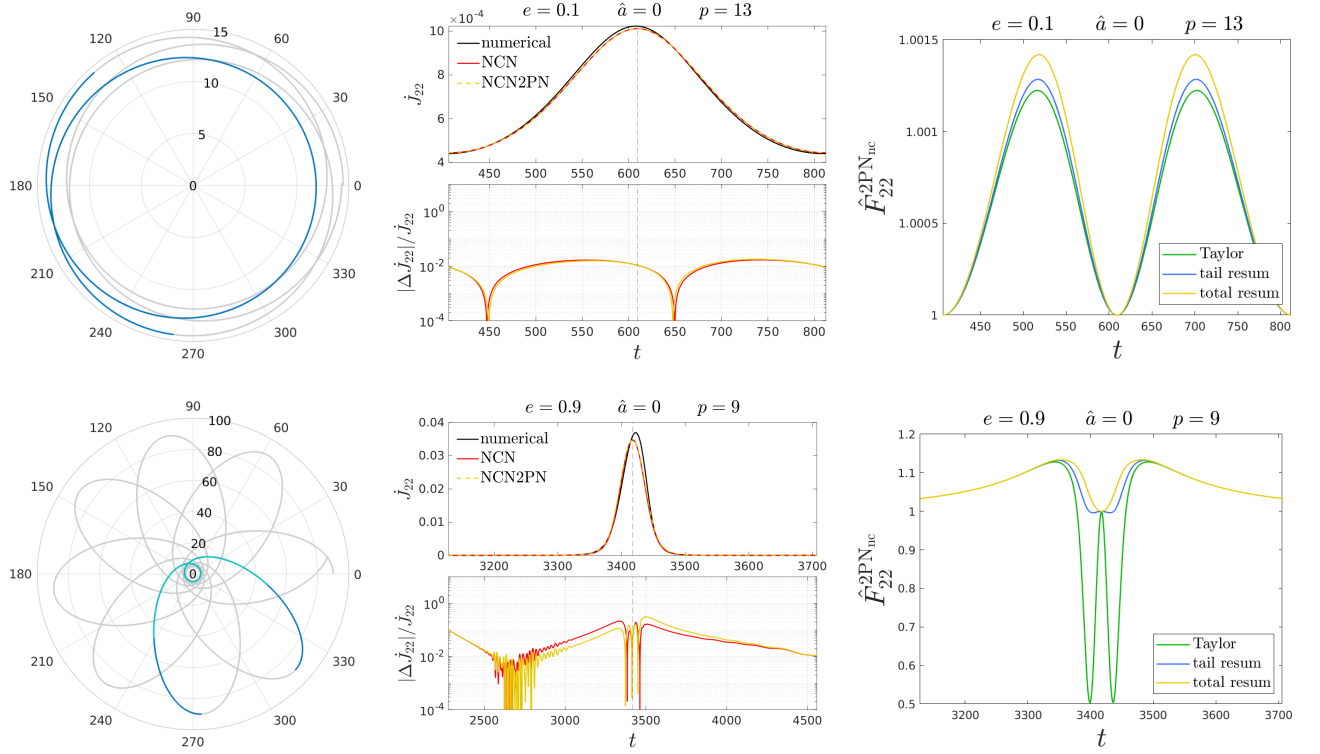


FIG. 12. Trajectories, quadrupolar angular momentum fluxes, and 2PN corrections to the flux as discussed in Sec VI. We show the standard flux from **TEOBResumS** (red), the result with 2PN resummed corrections (yellow), and the numerical flux (black). The corresponding analytical/numerical relative differences reported in the bottom panel are shown over the radial period; the corresponding part of the trajectories is highlighted in blue. On the rightmost panels we show the 2PN corrections to the flux in Taylor expanded form, with resummation of the tail factor and with resummation of both the instantaneous and hereditary parts. The latter is used for the 2PN flux of the middle panels. For the second configuration with $e = 0.9$, the fluxes and the 2PN corrections are shown over a time interval that is shorter than the radial period in order to highlight the burst of radiation at periastron; the corresponding part of the trajectories is highlighted in aqua-green.

while in the tail factor there are no ν -contributions and the two polynomials are

$$\hat{t}_{p_{r*}}^{1.5\text{PN}} = 1 + \frac{19094}{2661}y - \frac{127753}{13305}y^2 + \frac{22016}{887}y^3 - \frac{2569}{2661}y^4 - \frac{79250}{2661}y^5 + \frac{29231}{887}y^6 - \frac{204692}{13305}y^7 + \frac{7372}{2661}y^8, \quad (38)$$

$$\hat{t}_{p_{r*}}^{1.5\text{PN}} = 1 - \frac{4222}{443}y + \frac{115273}{11075}y^2 - \frac{74904}{2215}y^3 - \frac{15491}{2215}y^4 + \frac{91994}{2215}y^5 - \frac{77197}{2215}y^6 + \frac{169412}{11075}y^7 - \frac{7372}{2215}y^8. \quad (39)$$

Note that the analytical structure of the 2PN correction $\hat{F}_{22}^{2\text{PN}_{\text{nc}}}$ is similar to the one of the 2PN corrections to the waveform multipoles discussed in Ref. [21]. As already argued for the waveform, the polynomials in the y variable need to be resummed in order to provide reliable results in strong field regimes. We use diagonal Padé approximants for the polynomials in the tail and in the 2PN instantaneous part, while we leave in Taylor-

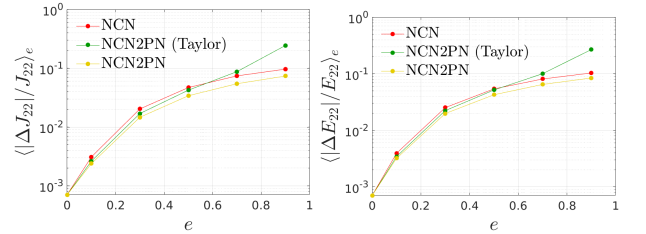


FIG. 13. Means of the analytical/numerical relative differences of the averaged fluxes, graphical representation of Table II. The mean $\langle \dots \rangle_e$ is performed over all the simulations with the same eccentricity. Since we consider two semilata recta for each pair (e, \hat{a}) and $\hat{a} = (0, \pm 0.2, \pm 0.6, \pm 0.9)$, each point is an average over 14 configurations.

expanded form the polynomials in the 1PN instantaneous contribution.

TABLE II. Averaged analytical/numerical relative differences for averaged quadrupolar fluxes, $\langle \delta F_{22} \rangle = \langle |\Delta F_{22}|/F_{22} \rangle$. We consider the fluxes computed using NCN, NCN with 2PN corrections in Taylor expanded form, and NCN2PN that includes 2PN noncircular corrections in resummed form. For each flux we compute the averages over the simulations with same eccentricity, the average for the nonspinning configurations, and the average for all the configurations. The values are reported in percentages. The relative difference averaged over the circular cases is $\langle \delta J_{22} \rangle_c = \langle \delta E_{22} \rangle_c = 0.07\%$. The averages at fixed eccentricity are shown in Fig. 13.

[%]	NCN		NCN2PN (Taylor)		NCN2PN	
	$\langle \delta J_{22} \rangle$	$\langle \delta E_{22} \rangle$	$\langle \delta J_{22} \rangle$	$\langle \delta E_{22} \rangle$	$\langle \delta J_{22} \rangle$	$\langle \delta E_{22} \rangle$
$e = 0.1$	0.31	0.39	0.26	0.34	0.24	0.32
$e = 0.3$	2.03	2.52	1.70	2.23	1.47	1.98
$e = 0.5$	4.70	5.41	4.24	5.17	3.40	4.26
$e = 0.7$	7.41	8.10	8.75	10.05	5.45	6.49
$e = 0.9$	9.66	10.36	24.36	26.91	7.37	8.44
$\hat{a} = 0$	3.01	3.21	4.85	5.53	1.59	1.98
all	4.03	4.48	6.56	7.46	3.00	3.59

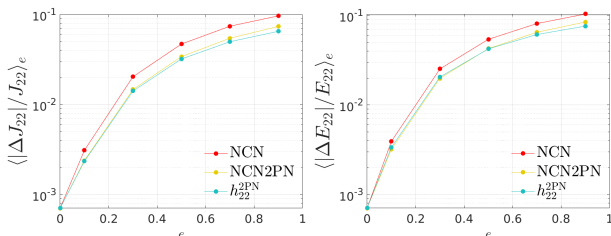


FIG. 14. Means of the analytical/numerical relative differences of the averaged fluxes. The mean $\langle \dots \rangle_e$ is performed over all the simulations with the same eccentricity. Since we consider two semilata recta for each pair (e, \hat{a}) and $\hat{a} = (0, \pm 0.2, \pm 0.6, \pm 0.9)$, each point is an average over 14 configurations. We report the results for the NCN and NCN2PN fluxes, and also for the fluxes computed from the 2PN waveform of Ref. [21] using Eqs. (27).

C. Testing the 2PN noncircular correction in Newtonian-factorized angular radiation reaction

We test the reliability of the resummed factor \hat{F}_{22}^{2PN} in the test-mass limit, focusing on the quadrupolar contributions to the angular momentum and energy fluxes, \dot{J}_{22} and \dot{E}_{22} . We start by considering two nonspinning configurations with eccentricities $e = 0.1, 0.9$ in Fig. 12. In the rightmost panels we show the 2PN noncircular correction $\hat{F}_{22}^{2PN_{nc}}$ with different resummation procedures: in Taylor expanded form (green), with resummation only on the hereditary part $\hat{F}_{22}^{2PN_{nc,tail}}$ (blue), and with resummation on both $\hat{F}_{22}^{2PN_{nc,inst}}$ and $\hat{F}_{22}^{2PN_{nc,tail}}$ (yellow). The latter is used in the radiation reaction (and fluxes) that we label as NCN2PN. In the case with $e = 0.1$, the three 2PN circular corrections are similar, while in the other con-

figuration with $e = 0.9$ the effects of the resummation become relevant. It is also possible to see that the resummation is more relevant for the hereditary part than for the instantaneous factor. This is a consequence of the fact that $\hat{t}_{p_{r_*}}^{1,5PN}$ are eighth-order y -polynomials, while $\hat{f}_{p_{r_*}}^{2PN}$ are fourth-order. However, the contribution of the resummed correction to \dot{J}_{22} is small even for $e = 0.9$, as shown in the middle panels of Fig. 12.

Deeper insight to the problem is obtained considering the analytical/numerical relative differences of the averaged quadrupolar fluxes and averaging over all the simulations with the same eccentricity, to obtain mean relative differences for each value of eccentricity, $\langle \Delta J_{22}/J_{22} \rangle_e$ and $\langle \Delta E_{22}/E_{22} \rangle_e$. In Table II and Fig. 13 we report these mean differences for three different radiation reactions: the standard prescription NCN, the prescription that includes in NCN the 2PN noncircular correction $\hat{F}_{22}^{2PN_{nc}}$ in Taylor-expanded form, and the prescription NCN2PN that includes the 2PN noncircular correction in NCN but with Padé resummation. As can be seen, the 2PN noncircular correction improves the radiation reaction NCN, but the resummation is needed in order to obtain more accurate results also for $e \gtrsim 0.6$. Indeed, for high eccentricity the periastron gets closer to the central black hole, making the y -polynomials of $\hat{F}_{22}^{2PN_{nc}}$ grow too much. The resummation prevents this issue and leads better results also for low eccentricity.

However, note that with the factorization scheme here proposed the post-Newtonian noncircular corrections cannot improve the analytical/numerical agreement at periastron and apastron, since at the two radial turning points we have $p_{r_*} = 0$ and $\hat{F}_{22}^{2PN_{nc}}$ reduces to unity. This could be an indication that using the EOB equations of motion at 2PN in the post-Newtonian noncircular corrections is not the best way to proceed, while leaving the explicit derivatives of coordinates and momenta could lead to more reliable fluxes. A first insight can be obtained computing the analytical fluxes considering Eqs. (27) and the waveform with resummed 2PN corrections⁵ proposed in Ref. [21]. As can be seen from Fig. 14, this procedure is practically consistent with the flux at 2PN order discussed above. The exploration of this different procedure and the inclusion of higher multipoles is left to future work.

VII. CONCLUSIONS

Future gravitational wave observations will further explore the astrophysical binary black holes populations [59–61], possibly also accessing sources with intermediate and extreme mass ratios [4–6]. One central issue for

⁵ More precisely, we consider the waveform with 2PN noncircular corrections where the noncircular tail factor and the instantaneous noncircular phase are resummed.

this science is the availability of faithful predictions of the complete gravitational waveform from the generic orbital motion and including the fast motion regime of the merger. The EOB is currently the only framework capable of predicting such waveforms for the entire range of astrophysical binaries, i.e. for generic mass ratios [9, 10, 12, 14, 62]. The radiation reaction force is one building block of any EOB model: while robust prescriptions for circularized binaries based on the factorized EOB waveform of Ref. [27] exist, less work has been done for generic orbits, e.g. [9, 10, 19]. Improving the current prescriptions for the EOB radiation reaction requires both new analytical information (PN results and EOB resummations) and exact numerical data (at least in some regimes). The test-mass limit is a critical benchmark: any analytical EOB structure must remain robust and accurate in this limit since this permits a continuum deformation of the model in the symmetric mass ratio and the calculation of the waveforms in different mass-ratio regimes. Yet this aspect is often overlooked when EOB models are tested. In this paper we assessed the performances of different EOB radiation reactions along generic planar orbits using the exact numerical result in the test-mass limit, e.g. Refs [14, 41, 42]. We considered three prescriptions put forward in the recent literature: (i) the quasicircular prescription (QC) of *SEOBNRv4HM* proposed for eccentric mergers in Ref. [20], (ii) the QC with 2PN noncircular corrections (QC2PN) proposed in Ref. [19], (iii) the QC corrected by the non-circular Newtonian prefactor (NCN) proposed in Ref. [9] and used in *TEOBResumS* [10, 13]. The main finding is that the NCN prescription performs best in reproducing the numerical results; this is a feature of almost all the cases analyzed in this work. This result is summarized in Fig. 6 and Table I. The test-mass results appear to carry over to the comparable-mass regime. Using a mildly eccentric (~ 0.2) numerical relativity simulation of equal-mass, nonspinning, binary merger we demonstrated that the NCN better captures the waveform phasing and frequency evolution than the QC prescription (see Figs. 9 and 11). In particular, the key issue is that the QC choice incorrectly circularizes the dynamics faster than the NCN prescription. By contrast, the latter remains more coherent with the NR data up to merger. The unphysical effect might be small on relatively short waveforms (~ 7 orbits) and practically gauged away in EOB/NR unfaithfulness computation thus yielding acceptable values ($\sim 1\%$). However, it is expected to build up over many GW cycles (as well as for larger eccentricities) eventually introducing systematics in the estimate of the parameters. Our result thus reiterates the importance of a detailed control of radiation reaction in the construction of EOB waveform models for eccentric inspirals. Given the lack of accurate NR simulations for eccentric inspirals with tenths of orbits, the use of test-mass limit data is the only method to validate current analytical prescriptions.

We also proposed an improved NCN2PN prescription that incorporates 2PN corrections in the flux following

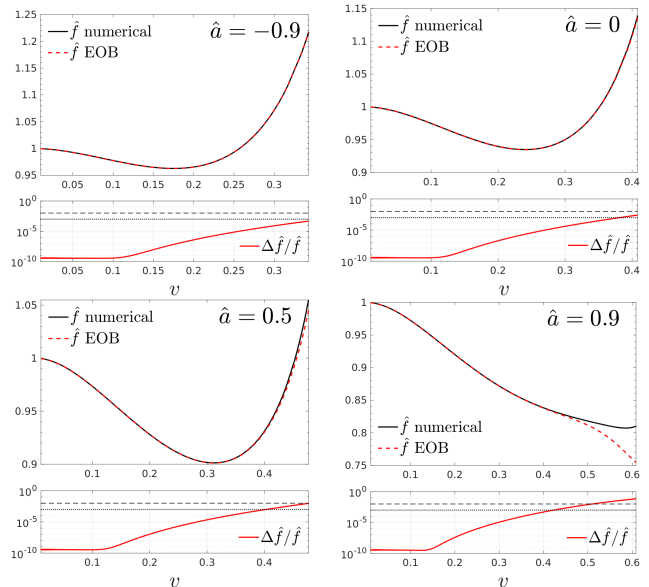


FIG. 15. Analytical/numerical comparisons of the Newton-normalized circular flux \hat{f} defined in Eq. (13) for four values of the Kerr spin parameter \hat{a} . The flux is plotted against $v = \Omega^{1/3}$, where Ω goes from zero to the orbital frequency of the last stable orbit. The two horizontal lines mark the 0.1% and the 1% thresholds. In the bottom panel we show the relative difference $(\hat{f}_{\text{num}} - \hat{f}_{\text{EOB}})/\hat{f}_{\text{num}}$.

the prescription of Ref. [21]. The latter has shown that high PN noncircular terms can be introduced within the waveform as a corrective multiplicative correction to the generic Newtonian prefactor. Focusing on the $\ell = m = 2$ mode we demonstrated here that applying an analogous procedure to the flux improves the agreement with the fluxes in the test-mass limit. The extension to higher modes as well as the inclusion in an improved EOB model with 2PN noncircular flux is postponed to future work.

VIII. ACKNOWLEDGMENT

We thank Astro Vitelli for continuous support during the development of this work. S.B. acknowledges support by the EU H2020 under ERC Starting Grant, No. BinGraSp-714626. M.O. and A.P. acknowledge support from the project “MOSAICO” financed by Fondo Ricerca di Base 2020 of the University of Perugia. M.O. and A.P. thank the Niels Bohr Institute for hospitality. Computations were performed on the “Tullio” server in Torino, supported by INFN.

Appendix A: Circular flux

In this Appendix we compare the circular flux with numerical frequency-domain circular data kindly provided to us by S. Hughes [63]. The comparisons of the analyti-

cal \hat{f} as defined in Eq. (13) with the numerical results are shown in Fig. 15 for different values of the spin \hat{a} . The frequency interval on which we plot the two quantities is $[0, \Omega_{\text{LSO}}]$, where Ω_{LSO} is the orbital frequency of the Last Stable Orbit (LSO). The analytical/numerical relative differences grow monotonically with the frequency, reaching the 0.25% at the LSO for $\hat{a} = 0$. Note that we are not considering the absolute value of the difference, so Fig. 15 also shows that the analytical circular flux is systematically slightly smaller than the numerical one. We also verified that the resummation of the ρ_{22} used through this paper for the test-mass fluxes⁶ leads to better analytical/numerical agreement than the ρ_{22} that is currently used in the comparable-mass case, which is the 5PN Taylor-expanded result with ν -contributions up to 3PN. Indeed while the former gives a difference at LSO of 0.25%, the latter gives 0.57%. Moreover, we also checked how the differences vary when including the higher multipoles. For the cases with $\hat{a} \lesssim 0$, the differences are almost independent of the number of multipoles used, while for

larger positive spins the inclusion of higher modes significantly changes the agreement. For example, in the case with $\hat{a} = 0.9$, the differences at LSO using only the (2,2) mode is 2.5%, but increases, respectively, to 7.4% and 7.0% if all the multipoles up to $\ell = 5$ and $\ell = 8$ are considered.

Appendix B: Explicit expressions for $\mathcal{F}_{\varphi,r}^{\text{ecc}}$

We report here the explicit expressions, in the test-mass limit, of the radiation reaction components $\hat{\mathcal{F}}_{\varphi}^{\text{ecc}}$ and $\hat{\mathcal{F}}_r^{\text{ecc}}$ that have been introduced in Ref. [19] and that we have recalled in Eq. (22). Separating the PN orders we have

$$\hat{\mathcal{F}}_{\varphi}^{\text{ecc}} = f_{\varphi,\text{ecc}}^{0\text{PN}} + f_{\varphi,\text{ecc}}^{1\text{PN}} + f_{\varphi,\text{ecc}}^{1.5\text{PN}} + f_{\varphi,\text{ecc}}^{2\text{PN}}, \quad (\text{B1})$$

$$\hat{\mathcal{F}}_r^{\text{ecc}} = f_{r,\text{ecc}}^{0\text{PN}} + f_{r,\text{ecc}}^{1\text{PN}} + f_{r,\text{ecc}}^{1.5\text{PN}} + f_{r,\text{ecc}}^{2\text{PN}}. \quad (\text{B2})$$

where

$$f_{\varphi,\text{ecc}}^{0\text{PN}} = \frac{29p_r^2 r - 10r^3 v_0^6 + 22}{12r^2 v_0^4}, \quad (\text{B3})$$

$$f_{\varphi,\text{ecc}}^{1\text{PN}} = \frac{1}{4032r^6 v_0^{10}} \left[-4928 - 13888p_r^2 r - 9744p_r^4 r^2 + \left(-28542r^3 - 74718p_r^2 r^4 + 6824p_r^4 r^5 \right) v_0^6 + \right. \\ \left. \left(27434r^4 + 36163p_r^2 r^5 \right) v_0^8 + \left(19638r^6 + 292p_r^2 r^7 \right) v_0^{12} - 12470r^7 v_0^{14} - 1132r^9 v_0^{18} \right], \quad (\text{B4})$$

$$f_{\varphi,\text{ecc}}^{1.5\text{PN}} = \frac{\pi}{1440r^4 v_0^7} \left[15390pr^2 + 10020pr^4 r - 49pr^6 r^2 + (210r^2 - 8910pr^2 r^3) v_0^6 - 210r^5 v_0^{12} \right] + \\ \frac{1}{288r^5 v_0^7} \left[-352\hat{a} - 2336\hat{a}p_r^2 r - 720\hat{a}p_r^4 r^2 + \left(904\hat{a}r^3 + 1482\hat{a}p_r^2 r^4 \right) v_0^6 - 552\hat{a}r^6 v_0^{12} \right], \quad (\text{B5})$$

$$f_{\varphi,\text{ecc}}^{2\text{PN}} = \frac{1}{1152r^7 v_0^{10}} \left[1408\hat{a}^2 p_r^2 r + 1856\hat{a}^2 p_r^4 r^2 + \left(4908\hat{a}^2 r^3 + 12080\hat{a}^2 p_r^2 r^4 \right) v_0^6 + \right. \\ \left. \left(-4356\hat{a}^2 r^5 - 5742\hat{a}^2 p_r^2 r^6 \right) v_0^{10} - 2532\hat{a}^2 r^6 v_0^{12} + 1980\hat{a}^2 r^8 v_0^{16} \right] + \\ \frac{1}{12192768r^{10} v_0^{16}} \left[12418560 + 53625600p_r^2 r + 77051520p_r^4 r^2 + 36832320p_r^6 r^3 + \right. \\ \left(34058304r^3 + 226443168p_r^2 r^4 + 248429664p_r^4 r^5 - 8358336p_r^6 r^6 \right) v_0^6 + \\ \left(-27653472r^4 - 77932512p_r^2 r^5 - 54678456p_r^4 r^6 \right) v_0^8 + \left(32614176r^6 + 111894048p_r^2 r^7 - \right. \\ \left. 730761696p_r^4 r^8 - 122683680p_r^6 r^9 \right) v_0^{12} + \left(-346723362r^7 - 889467642p_r^2 r^8 + \right. \\ \left. 58359600p_r^4 r^9 \right) v_0^{14} + \left(418059686r^8 + 551078677p_r^2 r^9 \right) v_0^{16} + \left(-226596384r^9 - \right. \\ \left. 428834448p_r^2 r^{10} - 141429456p_r^4 r^{11} \right) v_0^{18} + \left(212855418r^{10} - 8664156p_r^2 r^{11} \right) v_0^{20} - \\ \left. 190027130r^{11} v_0^{22} + \left(31642128r^{12} + 4003776p_r^2 r^{13} \right) v_0^{24} - 6419556r^{13} v_0^{26} + 55771632r^{15} v_0^{30} \right], \quad (\text{B6})$$

⁶ That is the one proposed in Ref. [38] and consists in resumming the ρ_{22} at 6PN after the factorization of the orbital contribution.

$$f_{r,\text{ecc}}^{0\text{PN}} = \frac{7p_r^2 r - 5r^3 v_0^6 + 11}{6r^2 v_0^4}, \quad (\text{B7})$$

$$f_{r,\text{ecc}}^{1\text{PN}} = \frac{1}{2016r^6 v_0^{10}} \left[-2464 - 5264p_r^2 r - 2352p_r^4 r^2 + \left(-14271r^3 - 30621p_r^2 r^4 - 1388p_r^4 r^5 \right) v_0^6 + \right. \\ \left. \left(13717r^4 + 8729p_r^2 r^5 \right) v_0^8 + \left(9819r^6 - 4654p_r^2 r^7 \right) v_0^{12} - 6235r^7 v_0^{14} - 566r^9 v_0^{18} \right], \quad (\text{B8})$$

$$f_{r,\text{ecc}}^{1.5\text{PN}} = \frac{\pi}{576r^2 v_0} \left[84 + 9376p_r^2 r + 5p_r^4 r^2 - 84r^3 v_0^6 \right] + \frac{r^5 v_0^7}{144} \left[-176\hat{a} - 112\hat{a}p_r^2 r + \right. \\ \left. \left(452\hat{a}r^3 + 606\hat{a}p_r^2 r^4 \right) v_0^6 - 276\hat{a}r^6 v_0^{12} \right], \quad (\text{B9})$$

$$f_{r,\text{ecc}}^{2\text{PN}} = \frac{1}{576r^7 v_0^{10}} \left[704\hat{a}^2 p_r^2 r + 448\hat{a}^2 p_r^4 r^2 + \left(2454\hat{a}^2 r^3 + 3160\hat{a}^2 p_r^2 r^4 \right) v_0^6 + \right. \\ \left. \left(-2178\hat{a}^2 r^5 - 1386\hat{a}^2 p_r^2 r^6 \right) v_0^{10} - 1266\hat{a}^2 r^6 v_0^{12} + 990\hat{a}^2 r^8 v_0^{16} \right] + \\ \frac{1}{6096384r^{10} v_0^{16}} \left[6209280 + 22579200p_r^2 r + 25824960p_r^4 r^2 + 8890560p_r^6 r^3 \right. \\ \left. + \left(17029152r^3 + 107258256p_r^2 r^4 + 105895440p_r^4 r^5 + 7160832p_r^6 r^6 \right) v_0^6 + \right. \\ \left. \left(-13826736r^4 - 29538936p_r^2 r^5 - 13198248p_r^4 r^6 \right) v_0^8 + \left(16307088r^6 + 75893328p_r^2 r^7 \right. \right. \\ \left. \left. - 291847248p_r^4 r^8 - 55172880p_r^6 r^9 \right) v_0^{12} + \left(-173361681r^7 - 364399587p_r^2 r^8 \right. \right. \\ \left. \left. - 19976940p_r^4 r^9 \right) v_0^{14} + \left(209029843r^8 + 133018991p_r^2 r^9 \right) v_0^{16} + \left(-113298192r^9 \right. \right. \\ \left. \left. - 151001928p_r^2 r^{10} - 82145448p_r^4 r^{11} \right) v_0^{18} + \left(106427709r^{10} - 53488818p_r^2 r^{11} \right) v_0^{20} - \right. \\ \left. 95013565r^{11} v_0^{22} + \left(15821064r^{12} - 15597792p_r^2 r^{13} \right) v_0^{24} - 3209778r^{13} v_0^{26} + 27885816r^{15} v_0^{30} \right]. \quad (\text{B10})$$

The expressions are written using the 0PN orbital velocity v_0 that reads

$$v_0 = \frac{(1 + \dot{p}_r r^2)^{1/6}}{\sqrt{r}}. \quad (\text{B11})$$

Appendix C: 2PN-accurate subleading flux multipoles

In Eq. (28) of the main text we showed the expression for the Taylor-expanded flux multipole $F_{22}^{2\text{PN}}$ which enters the factorization procedure described in Sec. VI. Here we list for completeness all the other flux multipoles that are relevant at 2PN accuracy:

$$F_{21}^{2\text{PN}} = -\frac{1}{c^2} p_\varphi^3 u^6 \frac{1-4\nu}{9} - \frac{1}{c^4} \left\{ p_\varphi^3 u^7 \left[\frac{5}{126} + \frac{13\nu}{63} - \frac{92\nu^2}{63} + p_\varphi^2 u \left(-\frac{85}{126} + \frac{335\nu}{126} + \frac{10\nu^2}{63} \right) \right] \right\}, \quad (\text{C1})$$

$$F_{31}^{2\text{PN}} = -\frac{1}{c^2} p_\varphi u^3 (1-4\nu) \left[u^2 \left(\frac{1}{24} - \frac{149p_\varphi^2 u}{2016} + \frac{11p_\varphi^4 u^2}{336} \right) + p_{r_*}^2 u \left(\frac{1}{336} + \frac{p_\varphi^2 u}{48} \right) - \frac{p_{r_*}^4}{84} \right] \\ + \frac{1}{c^4} p_\varphi u^4 (1-4\nu) \left\{ u^2 \left[\frac{2479}{6048} - \frac{31\nu}{189} + p_\varphi^2 u \left(-\frac{863}{1008} + \frac{559\nu}{2016} \right) + p_\varphi^4 u^2 \left(\frac{445}{1344} - \frac{347\nu}{4032} \right) \right. \right. \\ \left. \left. + p_\varphi^6 u^3 \left(\frac{47}{504} - \frac{55\nu}{2016} \right) \right] - p_{r_*}^2 u \left[\frac{73}{336} - \frac{31\nu}{168} + p_\varphi^2 u \left(-\frac{3779}{4032} + \frac{775\nu}{1344} \right) + p_\varphi^4 u^2 \left(\frac{51}{224} - \frac{3\nu}{14} \right) \right] \right\}$$

$$+ p_{r_*}^4 \left[\frac{59}{672} - \frac{13\nu}{672} + p_\varphi^2 u \left(-\frac{83}{224} + \frac{51\nu}{224} \right) \right] \Bigg\}, \quad (\text{C2})$$

$$F_{32}^{2\text{PN}} = -\frac{1}{c^4} p_\varphi^3 u^6 (1 - 3\nu)^2 \left[\frac{5}{126} u \left(1 + 7p_\varphi^2 u \right) - \frac{5}{252} p_{r_*}^2 \right], \quad (\text{C3})$$

$$\begin{aligned} F_{33}^{2\text{PN}} = & -\frac{1}{c^2} p_\varphi u^3 (1 - 4\nu) \left[u^2 \left(\frac{5}{8} + \frac{845p_\varphi^2 u}{224} + \frac{115p_\varphi^4 u^2}{112} \right) + p_{r_*}^2 u \left(\frac{5}{112} - \frac{205p_\varphi^2 u}{112} \right) - \frac{5}{28} p_{r_*}^4 \right] \\ & + \frac{1}{c^4} p_\varphi u^4 (1 - 4\nu) \left\{ u^2 \left[\frac{12395}{2016} - \frac{155\nu}{63} + p_\varphi^2 u \left(\frac{45175}{1008} - \frac{5065\nu}{288} \right) + p_\varphi^4 u^2 \left(\frac{66385}{4032} - \frac{37445\nu}{4032} \right) \right. \right. \\ & \left. \left. + p_\varphi^6 u^3 \left(\frac{265}{168} - \frac{335\nu}{672} \right) \right] - p_{r_*}^2 u \left[\frac{365}{112} - \frac{155\nu}{56} + p_\varphi^2 u \left(\frac{68195}{4032} - \frac{81685\nu}{4032} \right) + p_\varphi^4 u^2 \left(\frac{985}{224} - \frac{545\nu}{56} \right) \right] \right. \\ & \left. + p_{r_*}^4 \left[\frac{295}{224} - \frac{65\nu}{224} + p_\varphi^2 u \left(-\frac{545}{96} - \frac{3065\nu}{672} \right) \right] \right\}, \quad (\text{C4}) \end{aligned}$$

$$\begin{aligned} F_{42}^{2\text{PN}} = & -\frac{1}{c^4} p_\varphi u^4 (1 - 3\nu)^2 \left[u^2 \left(\frac{205}{4536} - \frac{5p_\varphi^2 u}{294} - \frac{575p_\varphi^4 u^2}{10584} + \frac{55p_\varphi^6 u^3}{1764} \right) - p_{r_*}^2 u \left(\frac{25}{588} - \frac{865p_\varphi^2 u}{10584} \right) \right. \\ & \left. + p_{r_*}^4 \left(\frac{10}{441} - \frac{65p_\varphi^2 u}{1764} \right) \right], \quad (\text{C5}) \end{aligned}$$

$$\begin{aligned} F_{44}^{2\text{PN}} = & -\frac{1}{c^4} p_\varphi u^4 (1 - 3\nu)^2 \left[u^2 \left(\frac{205}{648} + \frac{125p_\varphi^2 u}{42} + \frac{1115p_\varphi^4 u^2}{216} + \frac{145p_\varphi^6 u^3}{252} \right) - p_{r_*}^2 u \left(\frac{25}{84} + \frac{1705p_\varphi^2 u}{1512} \right. \right. \\ & \left. \left. + \frac{95p_\varphi^4 u^2}{42} \right) + p_{r_*}^4 \left(\frac{10}{63} - \frac{25p_\varphi^2 u}{252} \right) \right]. \quad (\text{C6}) \end{aligned}$$

Notice that, at the 2PN accuracy we are considering here, in all of the subleading flux multipoles only the instantaneous part survives. In other words, for these multipoles, the hereditary effects enter at higher orders than 2PN.

-
- [1] R. Abbott *et al.* (LIGO Scientific, Virgo), Phys. Rev. Lett. **125**, 101102 (2020), arXiv:2009.01075 [gr-qc].
- [2] V. Gayathri, J. Healy, J. Lange, B. O'Brien, M. Szczepanczyk, I. Bartos, M. Campanelli, S. Klimenko, C. Lousto, and R. O'Shaughnessy, (2020), arXiv:2009.05461 [astro-ph.HE].
- [3] R. Gamba, M. Breschi, G. Carullo, P. Retteno, S. Albanesi, S. Bernuzzi, and A. Nagar, Submitted to Nature Astronomy (2021), arXiv:2106.05575 [gr-qc].
- [4] P. Amaro-Seoane *et al.* (LISA), (2017), arXiv:1702.00786 [astro-ph.IM].
- [5] S. Babak, J. Gair, A. Sesana, E. Barausse, C. F. Sopuerta, C. P. L. Berry, E. Berti, P. Amaro-Seoane, A. Petiteau, and A. Klein, Phys. Rev. D **95**, 103012 (2017), arXiv:1703.09722 [gr-qc].
- [6] J. R. Gair, S. Babak, A. Sesana, P. Amaro-Seoane, E. Barausse, C. P. L. Berry, E. Berti, and C. Sopuerta, J. Phys. Conf. Ser. **840**, 012021 (2017), arXiv:1704.00009 [astro-ph.GA].
- [7] I. Hinder, L. E. Kidder, and H. P. Pfeiffer, (2017), arXiv:1709.02007 [gr-qc].
- [8] T. Hinderer and S. Babak, Phys. Rev. **D96**, 104048 (2017), arXiv:1707.08426 [gr-qc].
- [9] D. Chiaramello and A. Nagar, Phys. Rev. D **101**, 101501 (2020), arXiv:2001.11736 [gr-qc].
- [10] A. Nagar, P. Retteno, R. Gamba, and S. Bernuzzi, Phys. Rev. D **103**, 064013 (2021), arXiv:2009.12857 [gr-qc].
- [11] T. Islam, V. Varma, J. Lodman, S. E. Field, G. Khanna, M. A. Scheel, H. P. Pfeiffer, D. Gerosa, and L. E. Kidder, (2021), arXiv:2101.11798 [gr-qc].
- [12] A. Nagar, A. Bonino, and P. Retteno, Phys. Rev. D **103**, 104021 (2021), arXiv:2101.08624 [gr-qc].
- [13] A. Nagar and P. Retteno, (2021), arXiv:2108.02043 [gr-qc].
- [14] S. Albanesi, A. Nagar, and S. Bernuzzi, Phys. Rev. D **104**, 024067 (2021), arXiv:2104.10559 [gr-qc].
- [15] X. Liu, Z. Cao, and Z.-H. Zhu, (2021), arXiv:2102.08614 [gr-qc].
- [16] Q. Yun, W.-B. Han, X. Zhong, and C. A. Benavides-Gallego, Phys. Rev. D **103**, 124053 (2021), arXiv:2104.03789 [gr-qc].
- [17] A. Tucker and C. M. Will, Phys. Rev. D **104**, 104023 (2021), arXiv:2108.12210 [gr-qc].
- [18] Y. Setyawati and F. Ohme, Phys. Rev. D **103**, 124011 (2021), arXiv:2101.11033 [gr-qc].
- [19] M. Khalil, A. Buonanno, J. Steinhoff, and J. Vines, Phys. Rev. D **104**, 024046 (2021), arXiv:2104.11705 [gr-qc].
- [20] A. Ramos-Buades, A. Buonanno, M. Khalil, and S. Ossokine, (2021), arXiv:2112.06952 [gr-qc].
- [21] A. Placidi, S. Albanesi, A. Nagar, M. Orselli, S. Bernuzzi, and G. Grignani, (2021), arXiv:2112.05448 [gr-qc].
- [22] A. Buonanno and T. Damour, Phys. Rev. **D59**, 084006 (1999), arXiv:gr-qc/9811091.
- [23] A. Buonanno and T. Damour, Phys. Rev. **D62**, 064015 (2000), arXiv:gr-qc/0001013.
- [24] T. Damour, P. Jaranowski, and G. Schafer, Phys. Rev. **D62**, 084011 (2000), arXiv:gr-qc/0005034 [gr-qc].
- [25] T. Damour, Phys. Rev. **D64**, 124013 (2001), arXiv:gr-qc/0103018.
- [26] T. Damour, P. Jaranowski, and G. Schäfer, Phys. Rev. **D91**, 084024 (2015), arXiv:1502.07245 [gr-qc].
- [27] T. Damour, B. R. Iyer, and A. Nagar, Phys. Rev. **D79**, 064004 (2009), arXiv:0811.2069 [gr-qc].
- [28] A. Nagar, G. Riemenschneider, G. Pratten, P. Retteno, and F. Messina, Phys. Rev. D **102**, 024077 (2020), arXiv:2001.09082 [gr-qc].
- [29] G. Riemenschneider, P. Retteno, M. Breschi, A. Albertini, R. Gamba, S. Bernuzzi, and A. Nagar, Phys. Rev. D **104**, 104045 (2021), arXiv:2104.07533 [gr-qc].
- [30] W. E. East, S. T. McWilliams, J. Levin, and F. Pretorius, Phys. Rev. **D87**, 043004 (2013), arXiv:1212.0837 [gr-qc].
- [31] R. Gold and B. Brügmann, Phys. Rev. **D88**, 064051 (2013), arXiv:1209.4085 [gr-qc].
- [32] R. Abbott *et al.* (LIGO Scientific, Virgo), Astrophys. J. Lett. **900**, L13 (2020), arXiv:2009.01190 [astro-ph.HE].
- [33] T. Damour, F. Guercilena, I. Hinder, S. Hopper, A. Nagar, *et al.*, (2014), arXiv:1402.7307 [gr-qc].
- [34] Z. Cao and W.-B. Han, Phys. Rev. **D96**, 044028 (2017), arXiv:1708.00166 [gr-qc].
- [35] X. Liu, Z. Cao, and L. Shao, (2019), arXiv:1910.00784 [gr-qc].
- [36] Y. Pan, A. Buonanno, R. Fujita, E. Racine, and H. Tagoshi, Phys. Rev. **D83**, 064003 (2011), arXiv:1006.0431 [gr-qc].
- [37] A. Nagar and A. Shah, Phys. Rev. **D94**, 104017 (2016), arXiv:1606.00207 [gr-qc].
- [38] F. Messina, A. Maldarella, and A. Nagar, Phys. Rev. **D97**, 084016 (2018), arXiv:1801.02366 [gr-qc].
- [39] A. Nagar, F. Messina, C. Kavanagh, G. Lukes-Gerakopoulos, N. Warburton, S. Bernuzzi, and E. Harms, Phys. Rev. **D100**, 104056 (2019), arXiv:1907.12233 [gr-qc].
- [40] C. Cutler, E. Poisson, G. J. Sussman, and L. S. Finn, Phys. Rev. **D47**, 1511 (1993).
- [41] S. Bernuzzi, A. Nagar, and A. Zenginoglu, Phys. Rev. **D84**, 084026 (2011), arXiv:1107.5402 [gr-qc].
- [42] E. Harms, S. Bernuzzi, A. Nagar, and A. Zenginoglu, Class. Quant. Grav. **31**, 245004 (2014), arXiv:1406.5983 [gr-qc].
- [43] A. Albertini, A. Nagar, P. Retteno, S. Albanesi, and R. Gamba, (2021), arXiv:2111.14149 [gr-qc].
- [44] A. Bohé *et al.*, Phys. Rev. **D95**, 044028 (2017), arXiv:1611.03703 [gr-qc].
- [45] R. Cotesta, A. Buonanno, A. Bohé, A. Taracchini, I. Hinder, and S. Ossokine, Phys. Rev. **D98**, 084028 (2018), arXiv:1803.10701 [gr-qc].
- [46] T. Damour and A. Nagar, Phys. Rev. **D90**, 044018 (2014), arXiv:1406.6913 [gr-qc].
- [47] P. Retteno, F. Martinetti, A. Nagar, D. Bini, G. Riemenschneider, and T. Damour, (2019), arXiv:1911.10818 [gr-qc].
- [48] A. Nagar, T. Damour, and A. Tartaglia, Class. Quant. Grav. **24**, S109 (2007), arXiv:gr-qc/0612096.
- [49] T. Damour and A. Nagar, Phys. Rev. **D76**, 064028 (2007), arXiv:0705.2519 [gr-qc].
- [50] R. W. O'Shaughnessy, Phys. Rev. D **67**, 044004 (2003), arXiv:gr-qc/0211023.
- [51] L. C. Stein and N. Warburton, Phys. Rev. D **101**, 064007 (2020), arXiv:1912.07609 [gr-qc].
- [52] D. Bini and T. Damour, Phys. Rev. **D86**, 124012 (2012),

- arXiv:1210.2834 [gr-qc].
- [53] S. Teukolsky, Phys.Rev.Lett. **29**, 1114 (1972).
 - [54] S. A. Teukolsky, Astrophys. J. **185**, 635 (1973).
 - [55] Y. Kojima and T. Nakamura, Progress of Theoretical Physics **72**, 494 (1984).
 - [56] N. E. Rifat, G. Khanna, and L. M. Burko, Phys. Rev. Research. **1**, 033150 (2019), arXiv:1910.03462 [gr-qc].
 - [57] J. Thornburg, B. Wardell, and M. van de Meent, Phys. Rev. Res. **2**, 013365 (2020), arXiv:1906.06791 [gr-qc].
 - [58] “SXS Gravitational Waveform Database,” <https://data.black-holes.org/waveforms/index.html>.
 - [59] B. P. Abbott *et al.* (LIGO Scientific, Virgo), Phys. Rev. **X9**, 031040 (2019), arXiv:1811.12907 [astro-ph.HE].
 - [60] R. Abbott *et al.* (LIGO Scientific, Virgo), Phys. Rev. X **11**, 021053 (2021), arXiv:2010.14527 [gr-qc].
 - [61] R. Abbott *et al.* (LIGO Scientific, VIRGO, KAGRA), (2021), arXiv:2111.03606 [gr-qc].
 - [62] N. Yunes, A. Buonanno, S. A. Hughes, Y. Pan, E. Barausse, *et al.*, Phys.Rev. **D83**, 044044 (2011), arXiv:1009.6013 [gr-qc].
 - [63] A. Taracchini, A. Buonanno, S. A. Hughes, and G. Khanna, Phys.Rev. **D88**, 044001 (2013), arXiv:1305.2184 [gr-qc].